Noise Reduction in Qubit Readout with a Two-Mode Squeezed Interferometer

G. Liu,[*,†] X. Cao⊚,[†] T.-C. Chien, C. Zhou, P. Lu⊚, and M. Hatridge⊚[‡]

Department of Physics and Astronomy, University of Pittsburgh, Pittsburgh, Pennsylvania 15260, USA

Fault-tolerant quantum information processing with flawed qubits and gates requires highly efficient, quantum nondemolition qubit readout. In superconducting circuits, qubit readout using coherent light with fidelity above 99% has been achieved by using quantum limited parametric amplifiers such as the Josephson parametric converter (JPC). However, further improvement of such measurement faces many challenges, including the vacuum fluctuation of the coherent light that limits measurement fidelity. In this work we demonstrate dispersive qubit readout with a two-mode squeezed light interferometer formed by two JPCs. The first JPC generates two-mode squeezed vacuum at its output, which is coherently recombined by the second JPC after one branch is phase shifted and displaced by its interaction with the qubit-cavity system on that arm of the interferometer. We observe a 31% improvement in the power signal-to-noise ratio (SNR) of projective readout after replacing vacuum fluctuation in the readout cavity with two-mode squeezed vacuum containing on average one photon. This demonstrates a more efficient way of improving SNR than by increasing readout power. Furthermore, we investigate the quantum properties of the two-mode squeezed light in the system through weak measurement. Surprisingly, we find that tuning the interferometer to be less projective increases the measurement efficiency relative to the optimum setting for projective measurement. These enhancements may enable remote entanglement with lower efficiency components in a system with qubits in both arms of the interferometer.

I. INTRODUCTION

For quantum computing, an essential requirement for all tasks including qubit state preparation, gate calibration and error detection for quantum error correction (QEC) is the ability to perform fast single-shot qubit measurement with high fidelity. Furthermore, for error correction and state preparation, the measurement should also be quantum nondemolition (QND)—the qubit state should not suffer additional back action or randomization during the measurement process [1]. In superconducting circuits, these requirements are fulfilled by the dispersive readout method. In this method, a pulse of coherent microwave light is sent into a cavity that is dispersively coupled to a qubit inside it [2,3]. The pulse experiences a qubit-state-dependent phase and/or amplitude shift that entangles the state of the pulse with the qubit. The state of the qubit is determined by measuring the pulse at room temperature after the signal is amplified by a chain of low noise amplifiers.

Fast high-fidelity single-shot dispersive readout has been achieved in superconducting circuits thanks to the use of Josephson-junction-based parametric amplifiers (JPAs) as the first amplifier in the amplification chain [4–7]. These amplifiers provide high gain while adding only the minimum amount of noise to the signal required by quantum mechanics. For a given pulse amplitude, the signal-to-noise ratio (SNR) of the readout is thus fundamentally limited by the quantum fluctuation of the measurement light and the added noise of the JPA, which is half a photon for phase-preserving amplification [8]. Consequently, large SNR and high fidelity can be achieved in single-shot qubit readout with pulses containing just a few microwave photons. In the meantime, the QND requirement is satisfied as the readout photon number is much smaller than the critical photon number at which the dispersive coupling breaks down [3].

Although state-of-the-art dispersive readout is sufficient for small quantum circuits, the implementation of large quantum circuits (such as a error corrected machine) requires readout with higher fidelity as the probability of measuring all qubits correctly in a circuit decreases exponentially with the number of qubits. For example, in recent

---

*These authors contributed equally.

†gangqiang.liu@yale.edu

‡hatridge@pitt.edu

demonstrations of error suppression in QEC with qubit encoding [9,10], readout error is the dominant error that prevents these experiments from achieving break even. Although break even has been achieved in QEC with bosonic encoding [11,12], further improvements in readout are needed for performing tasks of practical importance with these codes.

Readout error typically arises from two sources: qubit decoherence (change of the qubit state) during the readout, and the overlapping support of probability distributions of measurement results corresponding to different qubit states that causes state assignment error. Substantial reduction of qubit decoherence error in readout now seems possible thanks to recent progress in fabricating superconducting qubits with near millisecond coherence times [13–15]. However, state assignment error in readout due to finite SNR is independent of the qubit coherence time and thus will be the dominant error source in circuits with these long coherence time qubits.

It might seem straightforward to improve readout SNR by increasing the readout power, but this can lead to other unwanted effects that degrade the readout quality and qubits' coherence. One well-known yet poorly understood effect is the reduction of qubit T_1 with increasing measurement strength, which leads to reduction in measurement fidelity and QNDness [16]. In certain cases, such an effect has been observed in readout with as few as 2.5 photons [17–19]. Recent works seem to indicate that this effect is intrinsic to driven nonlinear multilevel systems [20–27]. Although this effect might be alleviated with judiciously chosen system parameters, there will always be a fundamental limit on readout power.

In this work, we focus on improving SNR by circumventing the quantum mechanical limits on noise in qubit readout with coherent light. One method to achieve this is to use squeezed light to reduce noise inside the signal. Single-mode squeezed light has long been used in quantum metrology, in particular in interferometry of which the most famous example is the gravitational wave detector, to achieve measurement precision beyond the standard quantum limit set by the quantum fluctuations in coherent states of light [1,28–32]. It is therefore natural to expect that dispersive qubit readout could also be improved by using single-mode squeezed light. However, dispersive coupling will induce a qubit-state-dependent rotation of the squeezing axis, therefore mixing amplified noise of the antisqueezed quadrature into the squeezed quadrature of the single-mode squeezed light [33]. Furthermore, optimal dispersive readout typically requires large rotation. Therefore, only modest SNR improvements have been achieved in dispersive qubit readout with single-mode squeezed light. To overcome this problem, a different readout mechanism, the so-called longitudinal readout, has been proposed in which the qubit state information is mapped to the cavity field displacement [34]. Despite recent progress

[35–37], implementation of this readout method remains a challenging task.

Here we demonstrate inteferometric qubit readout based on two-mode squeezed (TMS) light input states and phase-preserving amplification [33]. This measurement scheme is based on a Mach-Zehnder interferometer with active nonlinear beam splitters, which is commonly known as a SU(1,1) interferometer [38]. Two-mode squeezed light naturally forms a pair of Gaussian, entangled states that travel along two paths, and when recombined in a phase-preserving amplifier, which in the quantum limit naturally has two input and output ports [8,39], can achieve superior readout SNR (and hence fidelity) by lowering the output noise level through the destructive interference between the two modes. In contrast to qubit readout with single-mode squeezed light, this readout scheme is more broadly compatible with the dispersive qubit-cavity coupling and allows SNR improvement over a larger range of coupling strengths.

In the experiment, we take advantage of the fact that two-mode squeezing and phase-preserving amplification are the same process, using two nominally identical, single-ended Josephson parametric converters (JPCs) to generate and process two-mode squeezed light in the interferometer [6,39,40]. The qubit-cavity system is embedded in one arm of the interferometer, where it imbalances the system by imparting a qubit-state-dependent phase shift on light passing through that arm. To allow fair comparison with standard coherent pulse readout, we perform readout by a combination of TMS vacuum and a cavity displacement drive that enters the system through the cavity's weakly coupled port, and so is subjected to no interference effects. Thus, our overall readout scheme has fixed measurement strength and gain (20 dB), and only the noise is affected.

We reduce output noise power below the standard quantum limit by 40% through the destructive interference between the correlated TMS noise entering the JPC [8,41], resulting in a 31% improvement in power SNR compared to coherent light readout. Moreover, we explore the back action and SNR of weak measurements [42] in our TMS readout scheme. We find, to our surprise, that the observed quantum efficiency of measurement (that is, the fraction of qubit back action we can extract from the measurement record) [42–46] varies inversely with noise in the interferometer, so that "noisier" measurements are more faithful. While we lack a detailed theory to explain this effect, it has important implications for future work on multiqubit quantum measurements that play a central role in tasks such as error correction and entanglement generation.

II. EXPERIMENT SETUP

In our experiment the two-mode squeezed light is generated, analyzed, and amplified with JPCs (Fig. 1). A JPC
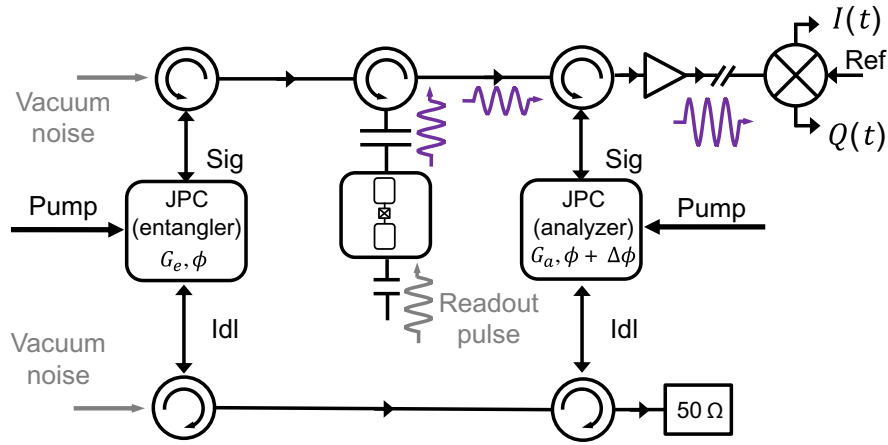
FIG. 1. Schematic of the experiment setup. Two nominally identical JPCs, entangler and analyzer, are connected by their signal (Sig) and idler (Idl) ports respectively with circulators and superconducting cables to form an interferometer. The unused ports on the circulators are terminated in cold 50 Ω loads that provide quantum vacuum noise to the entangler, and a dump for the unused signal on the lower arm of the interferometer. The upper arm of the interferometer is interrupted by a 3D transmon qubit-cavity system. The qubit measurement pulse is sent into the cavity via its weakly coupled port without going through both arms of the interferometer, which enables the switching between the two-mode squeezed light readout and coherent light readout *in situ* by turning on and off the pump of the entangler JPC. The signal is subsequently further amplified by a cryogenic HEMT and demodulated and recorded at room temperature.

is a nondegenerate phase-preserving amplifier based on the three-wave mixing process in a ring of four nominally identical Josephson junctions, known as a Josephson ring modulator (JRM). The JPC's Hamiltonian can be written as [6,39]:

$$\frac{H_{JPC}}{\hbar} = \omega_a a^\dagger a + \omega_b b^\dagger b + \omega_c c^\dagger c + g_3(a^\dagger b^\dagger c + abc^\dagger),$$

$$(1)$$

where a, b, and c are the annihilation operators of the three modes of the JPC that are refereed to as the "signal," "idler," and "common" mode, respectively, and g_3 is the three-wave coupling strength. Phase-preserving amplification is achieved by applying a strong microwave drive to the common mode at frequency $\omega_p \simeq \omega_a + \omega_b$. When ω_p is far detuned from ω_c, the pump is "stiff" in the sense that c can be replaced by its average value $\langle c \rangle e^{i\phi_p}$, where $\langle c \rangle$ and ϕ_p are the pump amplitude and phase, respectively. This reduces the three-wave mixing term to an effective two-wave coupling term between the signal and idler modes: $g_3\langle c\rangle(e^{i\phi_p}a^\dagger b^\dagger + e^{-i\phi_p}ab)$. As an amplifier, this device amplifies signals in reflection with an amplitude gain of $\sqrt{G}$, and in transmission with frequency conversion and an amplitude gain of $e^{i\phi_p}\sqrt{G-1}$.

The time evolution operator arising from phase-preserving gain is the so-called two-mode squeezing operator at a certain time [47]: $S = \exp(re^{-i\phi_p}ab + re^{i\phi_p}a^\dagger b^\dagger)$, where $re^{i\phi_p}$ is the complex squeezing parameter with $r = \cosh^{-1}\sqrt{G}$ [48,49]. Thus, the JPC, or any other nondegenerate phase-preserving amplifier, can also serve as a

generator of two-mode squeezed light with both spectral and spacial nondegeneracies [40,50].

In our experiment, we form an active interferometer with two nominally identical JPCs, the "entangler" and "analyzer," by directionally connecting their signal and idler ports [40] (Fig. 1). Uncorrelated vacuum noise enters the interferometer via the inputs of the entangler JPC, which transforms them into highly correlated, two-mode squeezed vacuum traveling along the two arms of the interferometer. These two paths recombine and interfere with each other in the analyzer JPC, generating outputs controlled by the gains and relative pump phase of the two JPCs. If both JPCs' pumps are applied with zero relative pump phase, the signal is simplify amplified twice, while a 180° relative pump phase will cause the analyzer JPC to deamplify the output of the entangler JPC. In the absence of loss and added noise, the output of the interferometer will return to uncorrelated vacuum if the gains of the two JPCs are matched and their pump phases are different by 180°.

We use the interferometer to read out a qubit by interrupting the upper arm with a microwave cavity, which in turn is dispersively coupled to a transmon qubit, as shown in Fig. 1. To achieve a superior SNR compared to qubit readout with coherent state input and phase-preserving amplification (CS + PP), the dispersive phase shift due to interaction with the qubit-cavity system must be either close to 0 or π, which correspond to the qubit-cavity dispersive shift χ being much smaller or larger than the cavity linewidth κ [33]. In our experiment, we design the quit-cavity system to have $\chi/\kappa = 0.19$, which

satisfies this requirement while also being favorable for fast readout (see Appendix A 2 for all the parameters of the experiment).

As we will discuss later, the noise produced by the interferometer when operated with no cavity displacement drive can itself carry qubit information for many combinations of entangler and analyzer gain and relative phase. However, high SNR readout requires a coherent drive to be applied to the cavity. The original theory proposal called for displacing the input to the upper arm of the entangler [33]; however, in this scenario the signal is both amplified and partially transmitted down both arms of the interferometer, so that there is interference in both the output signal and noise. This greatly complicates fair comparison with CS + PP readout, and so in our experiment we drive our readout through a second, weakly coupled port in the microwave cavity. The readout signal thus does not experience any form of interference, and experiences the same gain (from the analyzer only) in both our TMS and CS + PP readout. In this case, we squeeze only on the noise, with a degradation (enhancement) of SNR corresponding to a larger (smaller) output noise.

III. RESULTS

A. Generation and characterization of two-mode squeezed light

As a first step towards qubit readout with two-mode squeezed light, we demonstrate the generation and detection of such a nonclassical state [40]. As in previous demonstrations, the two-mode squeezed light is generated by displacing the two-mode squeezed vacuum produced by the entangler with a coherent drive applied to the weak port of the qubit-cavity system on the upper arm of the interferometer. Detection of the two-mode squeezed light is done by recording the output voltage from the signal port of the analyzer at room temperature as a function of the entangler pump conditions. As discussed earlier, only the noise of the output signal is expected to vary with the entangler pump, while the average amplitude should remain constant.

Figure 2(a) shows the variance (σ^2) of the output voltage signal, which is proportional to the noise power, normalized to that of unsqueezed inputs (coherent state readout; σ_{CS}^2) for entangler gain G_E between 0.7 and 4.5 dB and relative pump phase between 0° and 360°. The analyzer is operated with the pump condition that generates 20-dB gain when the entangler is off. This analyzer gain is chosen such that the noise power of its output signal is much stronger than those of the following amplifiers. The qubit is always prepared in the ground state ($|g\rangle$); therefore, it only contributes a constant phase shift to the total relative phase between the two arms of the interferometer.

As expected, the noise power of the output signal oscillates with relative pump phase and goes below that of the amplified coherent state noise power (indicated by the
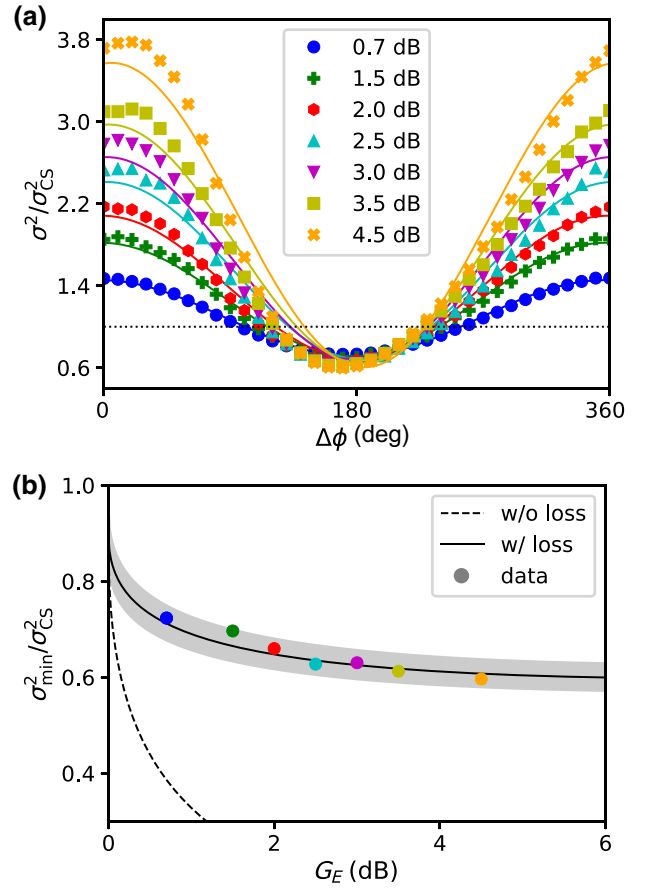

FIG. 2. Noise reduction in two-mode squeezed light. (a) Normalized output noise power of two-mode squeezed light as a function of relative pump phase $\Delta\phi$ for different entangler gains. The black dashed line represents the output noise level of the coherent vacuum (CS) input as a reference, while the other colors represent different entangler gains. Colored lines are fits to the data by our mode [Eq. (A22)] with analyzer gain as the fitting parameter. (b) Calculated optimal noise reduction without (dashed line) and with photon loss (solid line) for an analyzer gain of 19.4 dB. The shaded region represents results for an analyzer gain of 19.4 ± 0.3 dB. The colored dots represent optimal noise reductions extracted from (a).

dashed line) when the two pumps are out of phase. This oscillatory behavior, in particular the reduction of it by as much as 40% or 2.2 dB compared to that of the coherent state, is a direct manifestation of the entanglement between photons in the two arms of the interferometer. It is worth mentioning that the average amplitude of the output signal, as shown in Fig. 11(a) in Appendix A 4 d, also oscillates with the relative pump phase by $\pm 5\%$ rather than remaining constant. However, this phenomenon is independent of two-mode squeezing. It is due to analyzer gain variation caused by interference between its pump tone and the entangler pump leakage. This effect is analyzed in detail in Appendix A 3.

We fit these data with a model based on Ref. [40], which takes into account photon loss and noise added by later amplifiers, with analyzer gain being the only fitting parameter. These fits are shown in Fig. 2(a) as curves with the same color as their respective data set. For entangler gain below 3.5 dB, this model accurately captures the noise performance. At higher entangler gain, gain compression and other higher-order effects in the analyzer become important, causing deviation between the data and this model (see Fig. 11 in Appendix A 4 d). Measured optimal noise reduction ($\sigma_{min}^2/\sigma_{CS}^2$) as a function of entangler gain is shown in Fig. 2(b) (colored dots). It agrees well with the model prediction with an analyzer gain of 19.4 ± 0.3 dB (filled region). Without photon loss and noise from amplifiers after the analyzer, an optimal noise reduction by 90% could be achieved with an entangler gain of 4 dB and analyzer gain of 19.4 dB [Fig. 2(b), dashed line]. Although the achievable noise reduction is limited to 40%, it can translate into sizable SNR improvement and interesting measurement back action in qubit readout, as we show in the rest of the paper.

B. Qubit readout with two-mode squeezed vacuum

In order to utilize the two-mode squeezed light for qubit readout, we first study the effect of the dispersive qubit-cavity phase shift on the output noise of the interferometer. We repeat the measurements in Fig. 2 with $G_E = 2.0$ dB with the qubit now being prepared in either the ground ($|g\rangle$) or excited ($|e\rangle$) state, and show the results in Fig. 3(a). The oscillations of output noise with relative pump phase for the qubits in the ground and excited states are very similar, with a relative phase shift of 40° that is due to the qubit-state-dependent dispersive phase shift on photons traveling on the upper arm of the interferometer. For a given relative pump phase, this extra phase shift creates a qubit-state-dependent output noise power. This means that, except for the two relative phases ($\Delta\phi = 190°$ and 330°) where the output noise is identical for both qubit states, the output noise of the interferometer can measure or dephase the qubit state without explicitly displacing the cavity field, which is in sharp contrast with dispersive readout with CS + PP.

To demonstrate this dispersive qubit readout with only two-mode squeezed vacuum in the interferometer, we modify our measurement protocol by changing the initial state of the qubit to $(|g\rangle + i|e\rangle)/\sqrt{2}$, and adding a strong measurement after recording the noise output voltage to determine the state of the qubit after its interaction with the two-mode squeezed vacuum. As in Refs. [42,51], we construct a histogram where each pixel contains the average of all final measurement results of the z component of the qubit state Bloch vector conditioned on receiving a particular voltage (I_m, Q_m) in the measurement of the output noise.
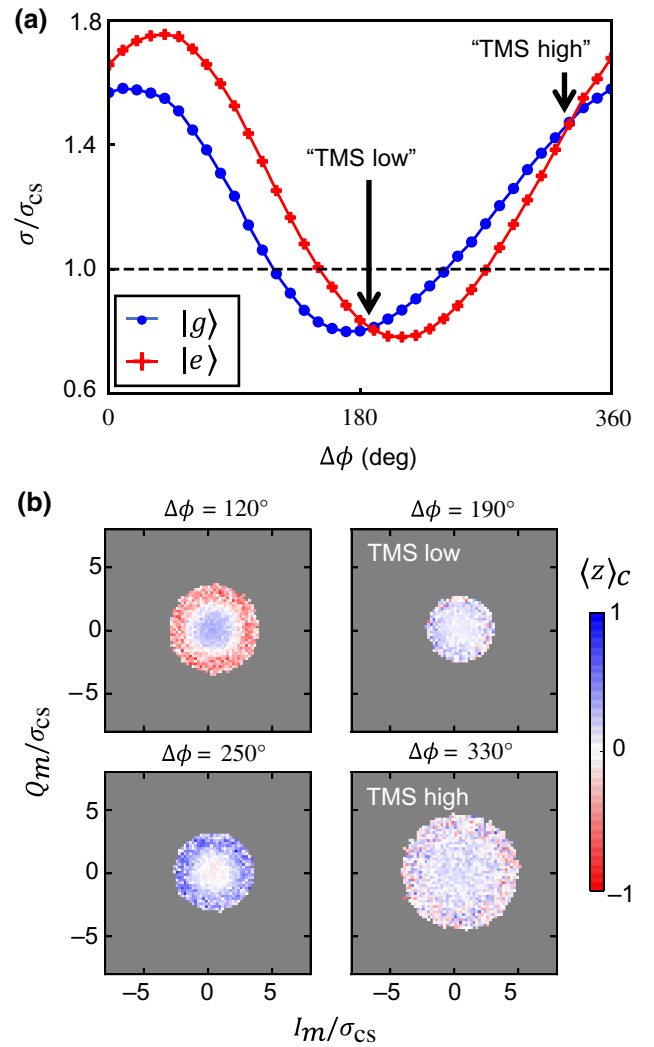

FIG. 3. Qubit readout with two-mode squeezed vacuum. (a) Normalized standard deviation of output noise voltage for two-mode squeezed vacuum input on the analyzer as a function of the relative pump phase and qubit state. The black dotted line shows the standard deviation when the input of the analyzer is the coherent (unsqueezed) vacuum. Blue and red curves represent results for two-mode squeezed vacuum noise recorded when the qubit is in the $|g\rangle$ and $|e\rangle$ states, respectively. (b) Conditional tomography data for the z component of the qubit Bloch vector after we record the output noise for 660 ns at different relative pump phases. The qubit is prepared in state $(|g\rangle + i|e\rangle)/\sqrt{2}$. The entangler gain is $G_E = 2.0$ dB and the analyzer gain is $G_A = 20$ dB.

In Fig. 3(b), we show the conditional z-axis tomography results at four different relative pump phases: $\Delta\phi = 120°$ and 250°, at which the difference between the output noise power for the qubits in the ground and excited states is the largest, and $\Delta\phi = 190°$ and 330°, at which the output noise powers for the qubits in the ground and excited states are the same. At $\Delta\phi = 120°$, we clearly see a "bullseye" pattern, with the qubit found to be in $|e\rangle$ if the recorded

noise voltage is large, and in $|g\rangle$ if the recorded noise voltage is small. A similar result is also seen at $\Delta\phi = 250°$, with the correspondence between the noise voltage and qubit states reversed.

These results show that two-mode squeezed vacuum in our interferometer, unlike unsqueezed vacuum, can entangle with the qubit state. An observer with a power meter could perform a readout of the qubit simply by measuring how much noise the circuit emits. This on average works poorly, as the two Gaussian distributions for the qubit states share a center, and so common outcomes near the origin poorly distinguish the qubit states (hence the pale central colors in the bullseyes). However, for outcomes far from the center, the contrast between the two distributions grows exponentially; for these outcomes, the qubit state is certain. The overall scheme closely resembles optical-frequency single-photon detection, in which a "click" outcome gives a definite result, while no click is ambiguous. This also implies that powering the entangler and analyzer will generate continuous qubit dephasing at these bias points. In contrast, at $\Delta\phi = 190°$ and $330°$ where the output noise levels are the same for different qubit states, similar to unsqueezed vacuum, no information about the qubit can be inferred from the system's noise output.

C. Qubit readout with two-mode squeezed light

We next show that the SNR of such measurements can be improved by using a fixed measurement tone and replacing the unsqueezed noise in the interferometer with two-mode squeezed fluctuations. The power SNR in our experiment is defined as

$$\mathrm{SNR} = \frac{(I_c^g - I_c^e)^2 + (Q_c^g - Q_c^e)^2}{\sigma_g^2 + \sigma_e^2}, \tag{2}$$

where $(I_c^{g(e)}, Q_c^{g(e)})$ is the center of the measurement result distribution when the qubit is in the $|g\rangle$ ($|e\rangle$) state and $\sigma_{g(e)}$ are the corresponding standard deviations.

To determine the SNR, we prepare qubits in the ground and excited states separately, and then perform readout by sending a coherent probe signal through the cavity from its weak port. Given that the coupling strength of the strong port is much greater than that of the weak port ($Q_{\mathrm{weak}} \gg Q_{\mathrm{strong}}$), quantum fluctuation of the cavity field will be set by either two-mode squeezed vacuum (entangler on) or vacuum (entangler off) entering from the strong port. With this setup, it is straightforward to obtain a fair comparison with standard CS + PP readout as there is ideally no interference in the average amplitude of the readout signals, and so any change in SNR will be solely due to changing the quantum noise in the interferometer.

In this experiment, the cavity drive strength is the same as that used in Fig. 2, which populates the cavity with

2.1 photons in steady state and gives a SNR of 0.9 in CS + PP readout. With this cavity drive strength, entangler gain as large as 3.5 dB can be used without causing significant analyzer gain compression [see Fig. 8(b) in Appendix A 3]. This allows us to perform qubit readout with the maximum amount of noise suppression achievable in our system (Fig. 2). It also allows us to characterize the measurement efficiency of these readout schemes with the weak measurement protocol under the same conditions, which will be discussed in the next section.

Figure 4(a) shows the SNR of two-mode squeezed light readout as a function of the relative pump phase ($\Delta\phi$) for different entangler gains. The data are normalized to the average SNR of CS + PP readout ($G_E = 0$ dB) with the same cavity drive strength. Improvement in the SNR, as
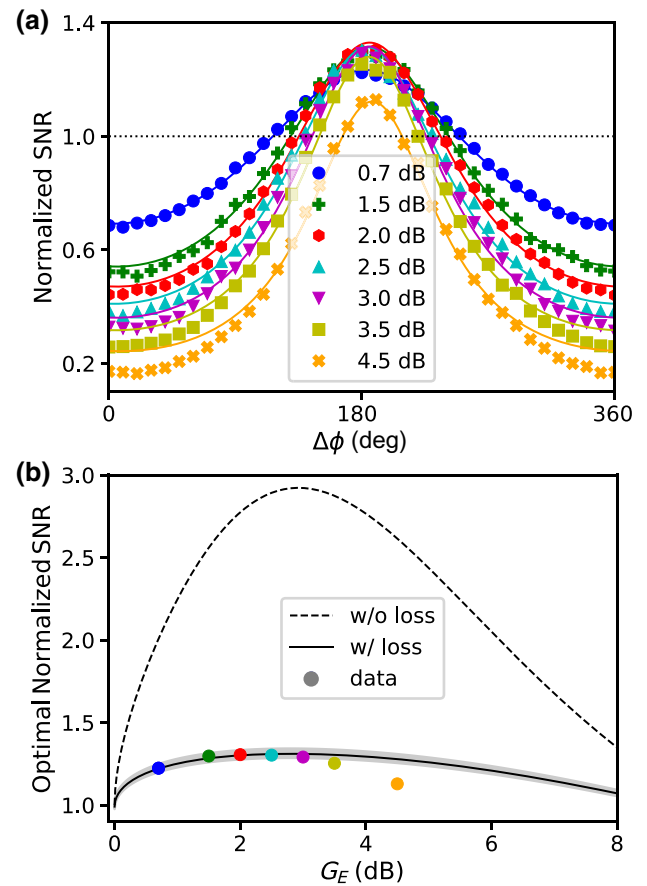

FIG. 4. SNR of qubit readout with two-mode squeezed light. (a) Normalized SNR of qubit readout with two-mode squeezed light for different entangler gains as a function of the relative pump phase. The colored symbols represent experiment data. The colored lines represent fitting to the data with our model [Eq. (A24)]. (b) Calculated optimal normalized SNR without (dashed line) and with (solid line) photon loss for an analyzer gain of 19.8 dB. The shaded region represents calculation results for analyzer gain between 19.5 dB (lower boundary) and 20.2 dB (upper boundary). Colored dots are optimal normalized SNRs extracted from the data set shown in (a) with the same color.

large as 31%, is observed for relative pump phases in the range of 140° to 240°. Outside this range, readout with two-mode squeezed light has a lower SNR than with coherent light due to one or both of the two-qubit states having a substantially higher noise than coherent light readout. These data are accurately reproduced (color curves) by a fit to our model with the analyzer gain as a fit parameter (Appendix A 4), with analyzer gain between 19.5 and 20.2 dB for $G_E \leq 3.5$ dB, and 17.9 dB for $G_E = 4.5$ dB, which accounts for analyzer gain compression under this entangler gain.

Optimal SNRs extracted from Fig. 4(a) are shown in Fig. 4(b) with respect to entangler gain. The dependence of optimal SNR on entangler gain is captured by our mode with an analyzer gain of 19.8 ± 0.3 dB (shaded area) except for $G_E = 4.5$ dB at which analyzer gain is reduced to 17.9 dB due to gain compression. As shown by both the data and theory, the optimal SNR improvement first increases to a maximum value of 31% for entangler gain between 2.0 and 3.0 dB, then decreases at higher entangler gain. This behavior results from the competition between better noise reduction at optimal pump phase—170° for $|g\rangle$ and 210° for $|e\rangle$—and faster noise rise away from it as entangler gain increases [Fig. 2(a)]. As shown in Fig. 4(a), optimal SNR is achieved with a relative pump phase of 190°, at which the total noise power for the qubits in states $|g\rangle$ and $|e\rangle$ is minimized. At low entangler gain ($G_E \leq 2$ dB), the total noise power at this relative pump phase decreases with increasing entangler gain, leading to an increasing SNR. However, as noise reduction at the optimal pump phase saturates at higher entangler gain, noise power at this relative pump phase would only increase, resulting in a decreasing SNR.

In the ideal case without photon loss and added noise from following amplifiers on the output line, the SNR of our system can be improved by as much as 190% with an entangler gain of 3 dB, as shown in Fig. 4(b) (dashed line). However, photon loss inside the interferometer limits the achievable SNR improvement to 72%, and noise added by following amplifiers on the output line further reduces it to 31%. Photon loss inside our system has been minimized by using components with the lowest loss that are commercially available, such as superconducting coaxial cables, and is on par with state of the art [40]. On the other hand, effects of photon loss and added noise on the output line can be alleviated by operating the analyzer with higher gain. For example, by operating the analyzer with 30-dB gain, instead of 20-dB gain, such effects would be reduced by a factor of 10, resulting in a SNR improvement of 43% instead of 31% with an entangler gain of 3 dB. Such an operation would require improvements to the analyzer compression power and bandwidth by factors of 10 and 3.2, respectively, which can be achieved by reducing the nonlinearity of the JPC and by increasing its coupling to the environment [7].

D. Quantum efficiency of a TMS light measurement

Another important figure-of-merit of a quantum measurement is its efficiency, which determines the fraction of information of the system being measured that is obtained by the observer, rather than lost to all other potential observers [3,42,45,52]. Readout fidelity scales exponentially with quantum efficiency, and thus it plays a vital role in experiments that require fast and high-fidelity measurements, such as feedback control in quantum error correction [53].

In our experiment, the quantum efficiency η of our qubit measurement is determined by analyzing its back action on the qubit with a weak measurement protocol established in Ref. [42]. This protocol provides a self-calibrated way of determining the overall efficiency of a measurement system. As there is no well-established theory for weak measurement back action with our TMS interferometer, we focus our study on two special cases where it most closely resembles the coherent light measurement; the "TMS high" and "TMS low" cases shown in Fig. 3(a) where the output noise power is independent of the qubit state, and the interferometer's output resembles CS + PP readout with unusual noise values.

In Fig. 5 we summarize the results of the back-action experiments with coherent light and two-mode squeezed light ($G_E = 0.5$ dB). Figure 5(a) shows the conditional x and y components of the qubit state Bloch vector for measurement results that have zero in-phase component ($I = 0$) of coherent light readout. In CS + PP readout, the x and y components of the qubit receive a purely quantum stochastic back action due to knowledge gained by the experimenter from the Q component of the readout pulse. This effect can also be present in readout with coherent states plus phase-sensitive amplification (CS + PS). In CS + PS readout, the choice of amplified quadrature can shift from granting the observer only I-quadrature information (which we would usually call an optimal readout quadrature), and correspondingly maximal z back action and no effect on the qubit's x and y components. By rotating the phase of the amplifier by 90°, we can reverse the situation, and produce only stochastic phase back action [45,54]. For CS + PP readout, these two back actions are equal in amplitude, as the amplifier favors neither quadrature. The amplitude and frequency of the x- and y-component oscillation, on the other hand, are determined by both the measurement strength and the efficiency of the measurement system. Therefore, by fitting this set of data, we can obtain the self-calibrated measurement strength and the overall efficiency of the measurement setup (see the Appendix for the detailed procedure). From the data shown in Fig. 5(a), we obtain an overall efficiency of $\eta = 0.46$ for the coherent light readout method that sets the base line of our system. By accounting for the known loss in coherence due to qubit T_2, we can also calculate a corrected efficiency of $\eta_{\mathrm{cor}} = 0.52$.
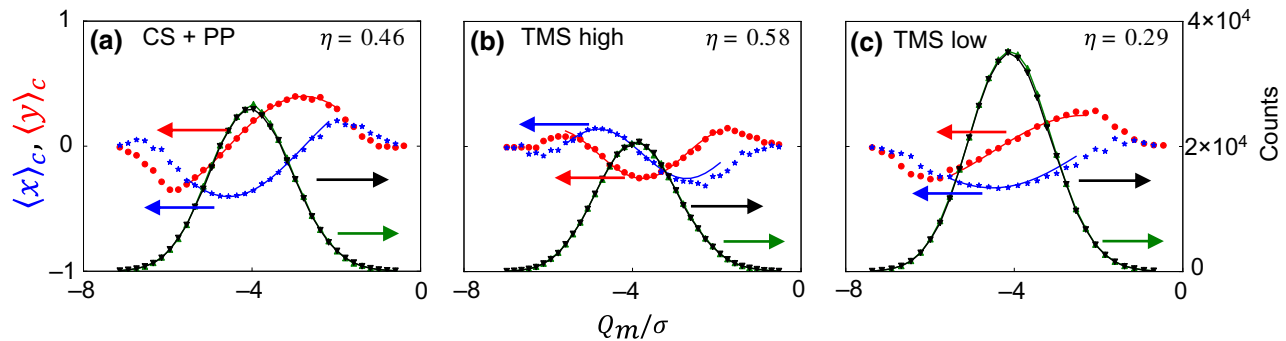
FIG. 5.   Quantum efficiency obtained by analyzing the back action of weak measurements. Tomography data for the *x* and *y* (blue stars and red dots) components of the qubit Bloch vector after we apply a weak measurement (see the Appendix for details) are plotted against the left axis. The counts observed for each *x* and *y* tomography data point are shown with black down-pointing triangles and green up-pointing triangles, plotted against the right axis. The data are recorded for coherent light as well as two-mode squeezed light at relative pump phase points such that the ground and excited state qubits have the same noise level. Data are then fitted to the theory model for coherent light [42]. The measurement strength is adjusted such that all the measurements have the same SNR. The efficiency value obtained for each point is shown as well. The η is the quantum efficiency extracted from the fitting model. A surprisingly low quantum efficiency is observed when the system has low output noise level.

Figures 5(b) and 5(c) show the results of applying the same protocol for two-mode squeezed light readout at the "TMS high" and "TMS low" matched noise points, respectively. We have adjusted the drive amplitudes to match all three measurement conditions' SNR (and correspondingly their *z*-component back action; see Fig. 15 in Appendix A 5). However, the data clearly show that both the oscillation frequency and amplitude of the *x* and *y* components are very different from the CS + PP case, which indicates that the back-action strength and quantum efficiency are very different. From the same fits, we obtain a quantum efficiency of 0.58 at the "TMS high" point, and 0.29 at the "TMS low" point.

The difference in the measurement efficiency with TMS light seems to be similar to the qubit readout with single-mode squeezed light and a phase-sensitive amplifier. For example, in Ref. [35], a similar reduction in quantum efficiency was observed when noise in the information-carrying quadrature is squeezed, which was explained as a consequence of an effective reduction in the quantum efficiency of the output chain following the quantum limited phase-sensitive amplifier; when quantum noise in the signal is reduced, the relative contribution of the fixed amount of noise added by the output chain is increased; thus, the quantum efficiency of the output chain is effectively reduced, and so is the overall quantum efficiency. However, this possible cause can be ruled out in our experiment. As shown in Fig. 16 in Appendix A 6, even if we vary the relative noise contributed by the analyzer and the output chain, the known changes in output noise cannot simultaneously explain the results at "TMS high" and "TMS low" points. The disagreement between our data and the theoretical estimation suggests that an intuitive explanation is not sufficient. The full quantum explanation of the problem remains an interesting question in quantum measurement theory to be addressed in future work.

IV. CONCLUSIONS AND OUTLOOK

In this work, we demonstrate a scheme for dispersive, interferometric readout of a superconducting qubit with two-mode squeezed light and phase-preserving amplification. In this readout scheme, we can increase the SNR of projective readout by suppressing the noise output of our amplifier below the usual Cave's limit for a phase-preserving amplifier fed with unsqueezed vacuum [8]. In our experiment, despite photon loss, we achieve a 31% improvement in the power SNR compared to standard coherent light plus phase-preserving amplification readout. With straightforward improvement in JPC compression power and bandwidth [7], we expect the SNR of our readout method to surpass the state of art of standard coherent light readout in next generation experiments. For multiplexed readout in large-scale superconducting circuits, our readout scheme can be implemented with a broadband two-mode squeezed light source such as traveling-wave parametric amplifiers [55,56] and impedance-matched broadband cavity-based JPAs [57,58].

A still more interesting result emerges as we investigate the quantum readout efficiency of our TMS interferometer using weak measurements at points where the noise output is the same for both qubit states. These data show that there are important effects on the ratio between *z* back action and the concomitant qubit phase back action of this measurement process relative to other known readout schemes. It appears that the increase in the SNR at the "TMS low" match point comes at the cost of reducing the trackability of phase back action. Conversely, at the "TMS high" match

point this phase trackability is enhanced. Although we rule out post-interferometer noise as the source of this effect, more theoretical work is needed to understand the role of inefficiencies inside the interferometer due to imperfect squeezing or amplification and losses in the interferometer arms. This limitation notwithstanding, the fact that the "TMS high" match point gives desirable quantum properties at a point that deliberately degrades the SNR and fidelity of the projective measurement should encourage exploration of measurement methods that are not just the quantum analogs of good classical measurement schemes.

Finally, while tracking a single qubit's phase during measurement is not of direct value for single-qubit measurements in quantum computing, measurement-based entanglement is a vital component of many error-correction schemes in quantum information, and in these schemes [51,59,60], maintaining or tracking two-qubit phase coherence during a high-fidelity measurement is vital. Our current experiment can be readily extended to two-qubit entanglement [59] by adding a second qubit on the lower arm, and we expect the ability to rebalance measurement strength and phase trackability *in situ* to give crucial tolerance for losses and inefficiencies that currently limit these experiments.

APPENDIX

1. Cryogenic microwave setup

The experiment is cooled down to around 20 mK on the base stage of a dilution refrigerator. The cryogenic microwave setup is shown in Fig. 6. Fridge input lines carrying signals from room temperature to the system are attenuated and filtered with homemade lossy Eccosorb filters. Room-temperature electronics, which include microwave generators, IQ mixers, and an arbitrary waveform generator, are used to produce microwave pulses to drive the qubit and cavity. Both the qubit and cavity drives are sent into the system through the qubit-cavity input line, which connects to the weak port of the cavity. The JPCs are pumped with the Keysight microwave generator. The output signal from the TMS interferometer is amplified by a chain of low noise cryogenic and room-temperature amplifiers before been down-converted, digitized, and demodulated with a room-temperature reference copy.

2. Sample parameters

The cavity in our experiment is a three-dimensional (3D) aluminum coaxial post cavity with a resonance frequency of $\omega_c/2\pi = 7.447$ GHz, coupling quality factors of $Q_{\mathrm{strong}} = 752$ on the strong port and $Q_{\mathrm{weak}} \sim 1\,000\,000$ on the weak port. Therefore, the cavity linewidth seen from the strong port is $\kappa/2\pi = 9.9$ MHz. The superconducting qubit is a 3D transmon qubit made by utilizing the commonly used Dolan bridge technique with a ground to excited state transition frequency of $\omega_{ge}/2\pi = 4.102$ GHz, anharmonicity $\alpha = 180$ MHz, and a qubit-cavity dispersive coupling strength of $\chi/2\pi = 1.8$ MHz. This qubit has a T_1 of 18.2 μs, and a T_{2R} of 4.4 μs (T_{2E} is 4.6 μs). The cavity is placed in an aluminum shield that is inside a μ-metal cryoperm shield. The whole system is wrapped in mylar.

3. Pump leakage cancelation and characterization

Because of the design of our JPC, the applied pump tone preferentially leaves from the signal and idler ports. Similarly, a pump tone can enter a JPC through its signal and idler ports (though in practice we apply pump tones only to the designated pump port). Thus, in our experiment, a fraction of the pump signal of each JPC always leaks into the other JPC through the arms of the interferometer. As both JPCs are biased such that their mode frequencies are matched, this pump leakage could severely affect its operation. Thanks to the directionality of the signal flow in the interferometer imposed by the circulators, pump leakage from analyzer JPC to entangler JPC is attenuated by -40 to -50 dB by the two circulators and can be safely neglected.

On the other hand, pump leakage from entangler JPC only experiences minimal attenuation on its path to analyzer JPC. Furthermore, analyzer JPC is operated with high gain (20 dB), which makes it extremely sensitive to pump power variations; to the first order of pump power, a relative pump power variation of Δp leads to a gain variation of $\sqrt{G}(\sqrt{G} + 1)^2 \Delta p$, namely a 1% variation of the pump power at $G = 100$ (20 dB) translates into a gain variation of $\Delta G = 10$ (0.4 dB). For example, with $G_E = 4$ dB and $G_A = 13$ dB at the interested frequency when they are turned on separately, we observe that G_A varies between 6 and 31 dB depending on the relative pump phase when both amplifiers are on, which corresponds to a ±50% variation of the pump power in analyzer JPC. Therefore, to ensure proper operation of the interferometer, it is crucial
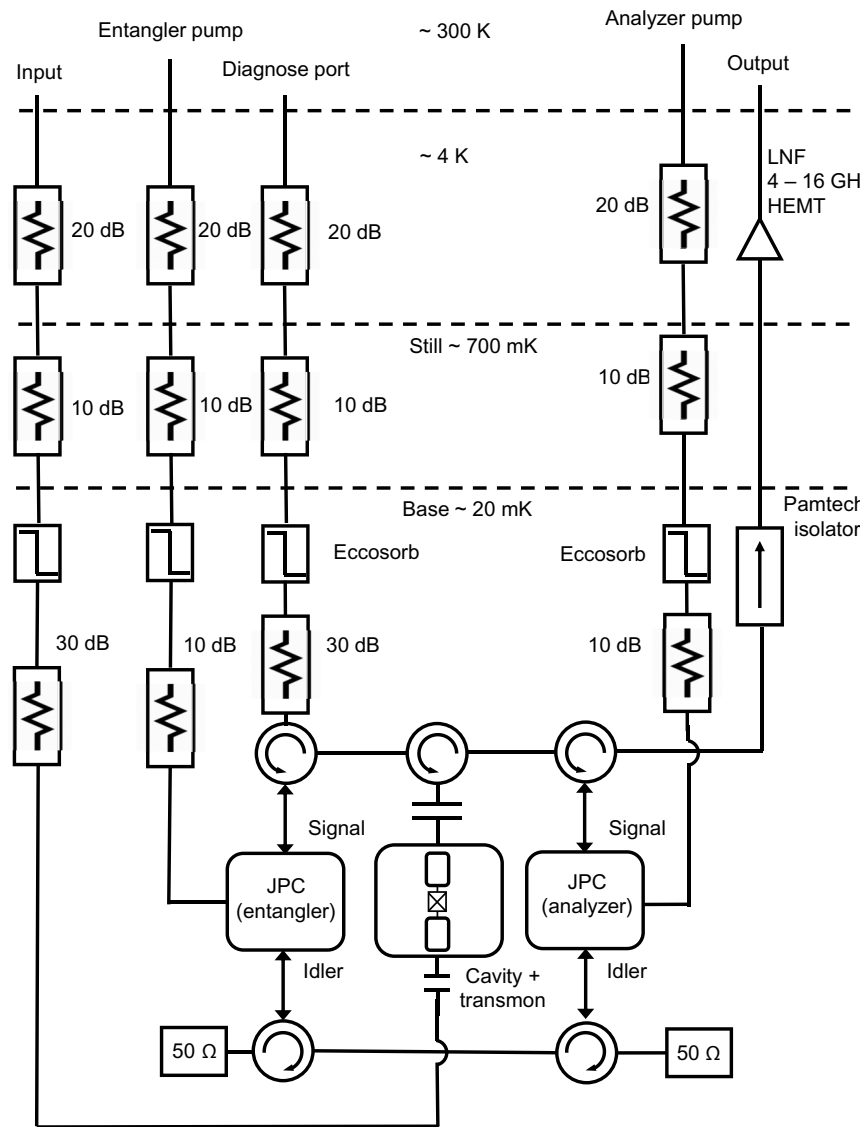
FIG. 6.   Wiring diagram of the cryogenic microwave measurement setup.

to minimize the pump power variation in the analyzer caused by entangler pump leakage.

To minimize the unwanted effect of entangler pump leakage, we deliver the pump signals to the JPCs through a circuit shown in Fig. 7, similar to that used in Ref. [40]. In this circuit, the entangler pump is split and fed to two IQ mixers that provide both JPC pumps. The analyzer's pump signal is a combination of the desired analyzer pump and a phase and amplitude shifted copy of the entangler pump that cancels its leakage in the analyzer JPC. Experimentally, we minimize the leakage by varying the analyzer pump phase and identifying the correction factor where analyzer gain is insensitive to the presence or absence of the entangler pump. Another way of eliminating the pump leakage to the analyzer could be to add low-pass filters on both arms of the interferometer. However, this would introduce additional loss to the interferometer and degrade

its performance. Therefore, we choose the active method described here. Furthermore, to prove that this effect is due entirely to pump leakage, and not two-mode squeezing effects in the interferometer, we verify the presence of pump leakage and our cancelation scheme with the upstream, entangler JPC tuned far away in frequency with flux.

To quantify the amount of residual pump leakage in the analyzer, we operate the analyzer at the 20-dB gain pump condition and measure the output signal strengths when a coherent drive is applied to the cavity weak port while sweeping the relative pump phase and entangler gain. Figure 8(a) shows the output signal strength normalized to that when the entangler is off for the qubit in $|g\rangle$. The oscillation of the output signal strength with relative pump phase manifests the interference between the residual entangler pump leakage and the analyzer pump. In this
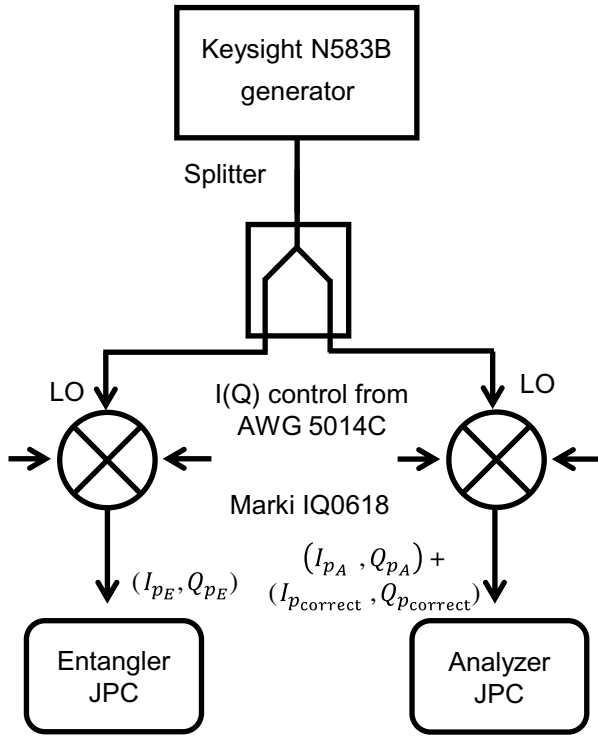
FIG. 7. Wiring diagram of the room-temperature setup for canceling the pump leakage. The output of a single generator (Keysight N583B) is split and fed to two IQ mixers that control the two JPC pumps. The signal applied to analyzer JPC is the sum of the desired pump and a correction designed to cancel leakage due to the entangler JPC pump. The use of a single generator has the additional benefit of stabilizing the relative phase of the two pumps, as a drift in phase of the generator affects both pumps equally.

case, the total time-averaged pump power in the analyzer can be written as

$$P = P_0(1 + \epsilon \cos(\Delta\phi + \phi_0) + \epsilon^2), \quad (A1)$$

where P_0 is the pump power of the analyzer pump, ϵ is the relative amplitude of the residual pump leakage, $\Delta\phi$ is the relative pump phase, and ϕ_0 is the constant phase shift between the pump leakage and the analyzer pump. The term ϵ^2 can be neglected in our analysis since $\epsilon \sim 0.01$. Consequently, the gain of the analyzer, to first-order dependence of the pump power, can be written as

$$G_A^{\text{TMS}} = G_A + \sqrt{G_A}(\sqrt{G_A} + 1)^2\epsilon \cos(\Delta\phi + \phi_0), \quad (A2)$$

where G_A is the gain of the analyzer without entangler pump leakage. The normalized output signal strength is

$$\frac{D^{\text{TMS}}}{D^{\text{CS}}} = \sqrt{\frac{G_A + \sqrt{G_A}(\sqrt{G_A} + 1)^2\epsilon \cos(\Delta\phi + \phi_0)}{G_A^{\text{CS}}}}, \quad (A3)$$
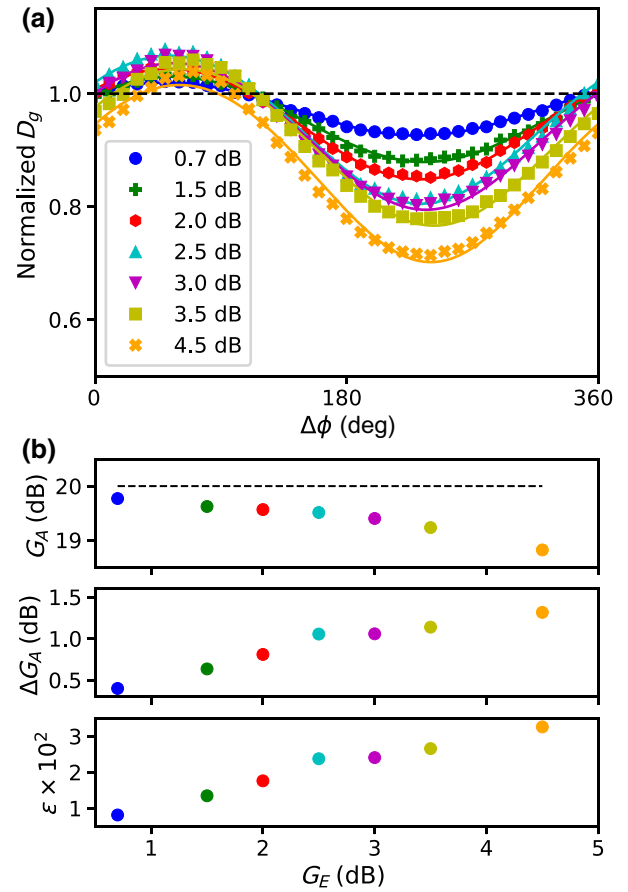

FIG. 8. Normalized signal strength of qubit readout with coherent light and displaced two-mode squeezed vacuum for the qubit in $|g\rangle$. (a) Average output voltage of a displaced two-mode squeezed vacuum state normalized to that of a coherent light state versus relative pump phase for different entangler gains. Data are represented by colored symbols and the corresponding theoretical fittings are represented by solid lines of the same color. (b) Analyzer gain (G_A), gain variation (ΔG_A), and relative amplitude of the entangler pump leakage (ϵ) versus entangler gain from fitting data in (a) with Eq. (A3). Color of the symbols represents entangler gain.

where $G_A^{\text{CS}} = 20$ dB is the analyzer gain when the entangler is off. By fitting data shown in Fig. 8(a) with Eq. (A3), we can get G_A and ϵ for given entangler gain. In Fig. 8(a) the fitting to the data of a given entangler gain is shown by solid lines of the same color. Figure 8(b) shows fitting results of G_A, ϵ, and maximum gain variation $\Delta G_A = \epsilon\sqrt{G_A}(\sqrt{G_A} + 1)^2$ with respect to the relative pump phase for all the different entangler gains.

The fitting gives an analyzer gain of $G_A = 19.7$ dB with the entangler on with gain $G_E \leq 3$ dB. The small reduction (0.3 dB) of the analyzer gain with the entangler on is a result of imperfect cancelation of the pump leakage. For entangler gain $G_E > 3$ dB, the analyzer gain decreases as a consequence of gain compression caused by increasing the power of the displaced TMS light. The residual entangler

pump power leakage also increases with the entangler gain from 0.01 to 0.03 of the analyzer pump power, which is 40 to 13 times smaller than that without the cancelation circuit.

4. Noise and SNR of qubit readout with the TMS interferometer

The generation and detection of TMS vacuum with two nondegenerate phase-preserving Josephson parametric amplifiers similar to JPC have been demonstrated in Ref. [40]. Here, we first summarize the relevant results from this work and then develop the theory for predicting the SNR improvement achievable in our experiment.

a. Gain of the TMS interferometer

The input and output of the two modes, a and b or signal and idler, of a phase-preserving amplifier (e.g., a JPC) is related by the scattering relations of the amplifier:

$$a_{\text{out}} = S^\dagger a_{\text{in}} S = \cosh r a_{\text{in}} + e^{i\phi} \sinh r b_{\text{in}}^\dagger, \quad (A4)$$

$$b_{\text{out}}^\dagger = S^\dagger b_{\text{in}}^\dagger S = e^{-i\phi} \sinh r a_{\text{in}} + \cosh r b_{\text{in}}^\dagger. \quad (A5)$$

Here $\cosh r = \sqrt{G}$ and $\sinh r = \sqrt{G-1}$ are the amplitude gains in reflection and in transmission, and ϕ is the phase of the pump tone. When two identical JPCs are respectively connected with their two ports, it is straightforward to calculate the scattering parameters for the combined system using the equations above twice. For example, the output field operator of the signal port of the second JPC, the "analyzer," is

$$a_{A,\text{out}} = S_{aa} a_{E,\text{in}} + S_{ab}^* b_{E,\text{in}}^\dagger \quad (A6)$$

with

$$S_{aa} = \cosh r_E \cosh r_A + e^{i\Delta\phi} \sinh r_E \sinh r_A, \quad (A7)$$

$$S_{ab} = e^{-i\phi_E}(\cosh r_A \sinh r_E + e^{-i\Delta\phi} \sinh r_A \cosh r_E), \quad (A8)$$

where ϕ_E, ϕ_A are the pump phases of the two amplifiers, and $\Delta\phi = \phi_A - \phi_E$ is the relative pump phase between them. Here S_{aa} and S_{ab} represent the amplitude gains of the input signals to the signal and idler ports of the first JPC, respectively. It is straightforward to see that the amplitudes of S_{aa} and S_{ab} will both vary with the relative pump phase $\Delta\phi$. When two JPCs have a matched gain ($r_E = r_A = r$) and a relative pump phase of π, the total gain of the system will become $\cosh^2 r - \sinh^2 r = 1$, indicating that the output signal power will be the same as the input signal. In the ideal case, when there is no loss and no added noise inside the interferometer, the output noise will just be the uncorrelated vacuum noise present at the input of the interferometer.

In practice, there is always photon loss inside amplifiers and along the paths between the two amplifiers. Without distinguishing these different loss mechanisms, we model photon loss in our TMS interferometer with beam splitters that partially transmit the incoming signal and couple uncorrelated noise from background thermal baths into the interferometer [40].

Figure 9(a) shows a schematic of our model of the interferometer. In order to accurately capture the effect of photon loss inside the TMS interferometer on qubit readout with TMS light, we use two beam splitters—before and after the qubit-cavity system—to model loss in the upper arm. Because of the symmetry of the upper arm with respect to the qubit-cavity system, the two beam splitters are identical. The power transmission coefficient of the beam splitters on the upper arm is η_a and that of the beam splitter on the lower arm is η_b. The qubit-cavity system is modeled as a phase shifter that adds a qubit-state-dependent phase shift θ_q on the upper arm, where $\theta_q = \theta$ for the qubit in $|g\rangle$ and $-\theta$ for the qubit in $|e\rangle$. The output at the signal port of the analyzer now becomes

$$a_{A,\text{out}} = S_{aa} a_{E,\text{in}} + S_{ab}^* b_{E,\text{in}}^\dagger + M_{aa} a_{\text{th}} + M_{ab}^* b_{\text{th}}^\dagger \quad (A9)$$
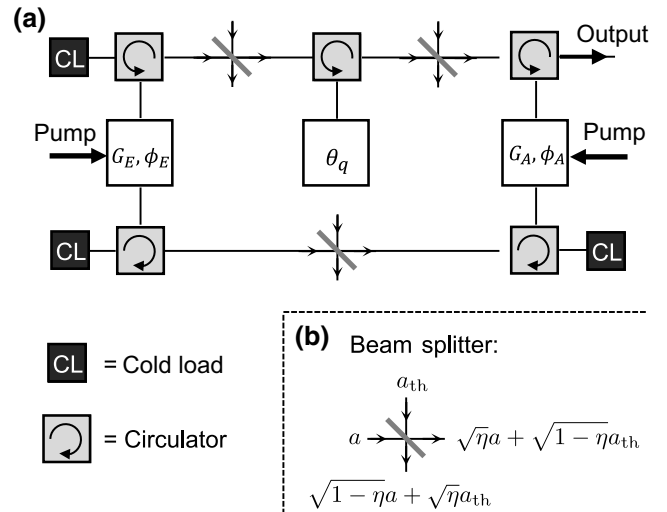
FIG. 9. Two-mode squeezed light interferometer with beam splitters representing loss in the signal pathway. (a) Entangler and analyzer JPCs are represented by squares with their gain and pump phase, respectively. Square with symbol θ_q represents the qubit-cavity system that introduces an extra qubit-state-dependent phase shift of θ_q to light propagating on the upper arm of the interferometer. (b) Photon loss is modeled by a beam splitter with power transmission coefficient η. It transforms the signal mode operators a and bath mode operator a_{th} of the same frequency into $\sqrt{\eta}a + \sqrt{1-\eta}a_{\text{th}}$ and $\sqrt{1-\eta}a + \sqrt{\eta}a_{\text{th}}$ in transmission, respectively.

with

$$
\begin{aligned}
S_{aa} = e^{i\Delta\phi}\big(& e^{i(\theta_q-\Delta\phi)}\eta_a \cosh r_A \cosh r_E \\
& + \sqrt{\eta_b}\sinh r_A \sinh r_E\big),
\end{aligned} \tag{A10}
$$

$$
\begin{aligned}
S_{ab} = e^{-i\phi_A}\big(& e^{-i(\theta_q-\Delta\phi)}\eta_a \cosh r_A \sinh r_E \\
& + \sqrt{\eta_b}\sinh r_A \cosh r_E\big),
\end{aligned} \tag{A11}
$$

$$
M_{aa} = (1+\sqrt{\eta_a}e^{i\theta_q})\sqrt{1-\eta_a}\cosh r_A, \tag{A12}
$$

$$
M_{ab} = e^{-i\phi_A}\sqrt{1-\eta_b}\sinh r_A. \tag{A13}
$$

Comparing to Eq. (A6), the two extra terms in Eq. (A9) represent the contribution of noise to the output signal. Comparing Eqs. (A7)–(A8) with Eqs. (A10)–(A11), we see that the loss in the interferometer indeed leads to a reduction in the gain of the input signal.

The qubit-cavity system, on the other hand, introduces a qubit-state-dependent phase shift between the two arms through which the qubit state information is encoded in the gain of the interferometer. If the qubit measurement signal enters the interferometer from the input port, the entangler [33], then both its average amplitude and fluctuation measured at the output of the analyzer would carry the qubit state information. However, this way of measuring the qubit state with TMS light has the drawback that the average amplitude of the signal is also reduced when the noise is reduced. This effectively reduces the SNR of the signal at room temperature since a fixed amount of noise will be added to it by the low noise amplifiers (LNAs) on the output line. In our experiment, the qubit measurement signal entering from the weak port of the cavity will only interact with the analyzer; therefore, the average amplitude of the output signal will be independent of the qubit state. Instead, the fluctuation or noise of the output signal will carry the qubit state information.

b. Noise of the TMS interferometer

In experiment, we measure both the in-phase (I) and quadrature (Q) components of the output signal, which are related to the field operators by

$$
I = \frac{a+a^\dagger}{2}, \qquad Q = i\frac{a^\dagger-a}{2}. \tag{A14}
$$

The noise power of the output signal is proportional to the variance of the signal σ^2, which is given by

$$
\sigma^2 = \sigma_I^2 + \sigma_Q^2 \tag{A15}
$$

with

$$
\begin{aligned}
\sigma_I^2 &= \langle I^2\rangle - \langle I\rangle^2 \\
&= \tfrac{1}{4}(\langle a^2\rangle - \langle a\rangle^2 + \langle a^{\dagger 2}\rangle - \langle a^\dagger\rangle^2) \\
&\quad + \tfrac{1}{2}(\langle a^\dagger a\rangle - \langle a^\dagger\rangle\langle a\rangle) + \tfrac{1}{4},
\end{aligned} \tag{A16}
$$

$$
\begin{aligned}
\sigma_Q^2 &= \langle Q^2\rangle - \langle Q\rangle^2 \\
&= -\tfrac{1}{4}(\langle a^2\rangle - \langle a\rangle^2 + \langle a^{\dagger 2}\rangle - \langle a^\dagger\rangle^2) \\
&\quad + \tfrac{1}{2}(\langle a^\dagger a\rangle - \langle a^\dagger\rangle\langle a\rangle) + \tfrac{1}{4}.
\end{aligned} \tag{A17}
$$

Under the condition that both the input fields of the entangler and the bath modes are in vacuum states, for the output of the signal mode of the analyzer, we have

$$
\sigma_{I,\text{out}}^2, \sigma_{Q,\text{out}}^2 = \tfrac{1}{2}\langle a_{A,\text{out}}^\dagger a_{A,\text{out}}\rangle + \tfrac{1}{4}. \tag{A18}
$$

From Eq. (A9), we get

$$
\begin{aligned}
\langle a_{A,\text{out}}^\dagger a_{A,\text{out}}\rangle &= \Big\langle\big(\alpha_1^* a_{E,\text{in}}^\dagger + \alpha_2 b_{E,\text{in}} + \alpha_3^* a_{\text{th}}^\dagger + \alpha_4 b_{\text{th}}\big) \\
&\qquad \times \big(\alpha_1 a_{E,\text{in}} + \alpha_2^* b_{E,\text{in}}^\dagger + \alpha_3 a_{\text{th}} + \alpha_4^* b_{\text{th}}^\dagger\big)\Big\rangle \\
&= |\alpha_2|^2\langle b_{E,\text{in}} b_{E,\text{in}}^\dagger\rangle + |\alpha_4|^2\langle b_{\text{th}} b_{\text{th}}^\dagger\rangle \\
&= |e^{i(\theta_q-\Delta\phi)}\eta_a \cosh r_A \sinh r_E \\
&\quad + \sqrt{\eta_b}\sinh r_A \cosh r_E|^2 + (1-\eta_b)\sinh^2 r_A \\
&= (\eta_a^2 \cosh^2 r_A + \eta_b \sinh^2 r_A)\sinh^2 r_E \\
&\quad + \frac{\eta_a\sqrt{\eta_b}}{2}\sinh 2r_A \sinh 2r_E \cos(\theta_q-\Delta\phi) \\
&\quad + \sinh^2 r_A.
\end{aligned} \tag{A19}
$$

Therefore,

$$
\begin{aligned}
\sigma_{I,\text{out}}^2, \sigma_{Q,\text{out}}^2 &= (\eta_a^2 \cosh^2 r_A + \eta_b \sinh^2 r_A)\frac{\sinh^2 r_E}{2} \\
&\quad + \frac{\eta_a\sqrt{\eta_b}}{4}\sinh 2r_A \sinh 2r_E \cos(\theta_q-\Delta\phi) \\
&\quad + \frac{\cosh 2r_A}{4}.
\end{aligned} \tag{A20}
$$

In the special case of $r_E = 0$, namely the entangler is off, the output noise photon number is $\cosh 2r_A/2$, which is the output noise of a quantum limited phase-preserving amplifier with vacuum noise input on its signal and idler port.

Equation (A20) gives the output noise photon number at the signal port of the analyzer. It is related to the noise photon number measured at room temperature by

$$
\sigma^2 = G_{\text{out}}(\sigma_{\text{out}}^2 + N_{\text{out}}), \tag{A21}
$$

where G_{out} is the total gain of the output line, N_{out} is the added noise photon number referred back to the input of the HEMT. Therefore, the ratio of TMS light noise output and coherent light noise output measured at room temperature is

$$
\frac{\sigma^2}{\sigma_{\text{CS}}^2} = \frac{\sigma_{\text{out}}^2 + N_{\text{out}}}{\cosh 2r_A/2 + N_{\text{out}}}. \tag{A22}
$$

c. SNR of qubit readout with the TMS interferometer

As defined in Eq. (2), the SNR of qubit readout is

$$\text{SNR} = \frac{(I_c^g - I_c^e)^2 + (Q_c^g - Q_c^e)^2}{\sigma_g^2 + \sigma_e^2}, \qquad \text{(A23)}$$

where the signal strength is given by the separation between the distributions of measurement results corresponding to qubits in $|g\rangle$ and $|e\rangle$. For a given qubit-cavity system, this separation is proportional to the strength of the measurement pulse and total amount of amplification. In our experiment, the strength of the measurement pulses are the same for TMS light and coherent light readout, and the total gain of the LNAs following the analyzer is constant; therefore, the ratio between the SNR of TMS light readout and coherent light readout recorded at room temperature is

$$\frac{\text{SNR}}{\text{SNR}_{\text{CS}}} = \frac{\sigma_g^2 + \sigma_e^2}{\sigma_{\text{CS,g}}^2 + \sigma_{\text{CS,e}}^2} \frac{G_A^{\text{TMS}}}{G_A^{\text{CS}}}, \qquad \text{(A24)}$$

where analyzer gain variation due to residual entangler pump leakage has been taken into account.

d. Photon loss inside the TMS interferometer

Equations (A22) and (A24) give expressions for noise and qubit readout SNR of TMS light normalized to that of coherent light. In order to compare their predictions to data, we need to know the following parameters: η_a, η_b, and N_{out}. In this section, we show how to determine these parameters in our experiment.

First, the ratio $\eta_a^2 \eta_b$ is determined by measuring S_{aa} [Eq. (A10)] with a vector network analyzer (VNA). In particular, S_{aa} is measured under four different conditions. (1) Both the entangler and analyzer are off; thus, $S_{aa} = e^{i\theta_q} \eta_a$. (2) The entangler is on and the analyzer is off; thus, $S_{aa} = e^{i\theta_q} \eta_a \cosh r_E$. (3) The entangler is off and the analyzer is on; thus, $S_{aa} = e^{i\theta_q} \eta_a \cosh r_A$. (4) The entangler and analyzer are both on; thus, S_{aa} takes the form in Eq. (A10).

Although it seems straightforward to determine η_a by measuring S_{aa} with both the entangler and analyzer off, the measurement result recorded at room temperature is $G_{\text{sys}} S_{aa}$ rather than S_{aa}, where G_{sys} is the total gain of the system that is determined by the total attenuation on the input line and total gain on the output line. To determine G_{sys}, separate measurements are needed. Therefore, a measurement under condition (1) alone cannot determine the value of η_a. However, it can be used to normalize the measurement results under conditions (2) and (3) to obtain the entangler gain ($\cosh^2 r_e$) and analyzer gain ($\cosh^2 r_A$), respectively. By combining these results with the measurement under condition (4), we can determine $\eta_a^2 \eta_b$.

We measured S_{aa} for a range of entangler gains $G_E = \cosh^2 r_E$ and pump phase differences $\Delta\phi$ while keeping the

analyzer gain to $G_A = \cosh^2 r_A = 10$ dB and the qubit in state $|g\rangle$. We perform this characterization measurement with relatively small analyzer gain (10 dB) to minimize the effect of gain variation due to entangler pump leakage, and unwanted higher-order effects in the analyzer.

As examples, Fig. 10 shows data for $G_E = 0.67$ and 9.15 dB. By fitting these data with Eq. (A10), we can extract the ratio of the transmission coefficient of the upper and lower arms, η_a^2/η_b, which is found to be 0.8. This imbalance in transmission between the two arms is mostly due to the insertion loss of the extra circulator and cables on the upper arm that connects to the qubit-cavity system. Typical insertion loss of this circulator (Qunistar 4 to 8 GHz cryogenic circulator) is 0.2 to 0.5 dB per pass, which would give 0.4 to 1.0 dB (0.1 to 0.2) of additional loss on the upper arm. We estimate that extra cables in the upper arm contribute to about 0.5 dB loss to the signal.

In order to determine the absolute values of η_a and η_b, in principle we would need to know G_{sys}—the total gain of the system—as discussed earlier. However, as the power transmission coefficients also represent the quantum efficiency of transmitting information with photons along these signal pathways, we can deduce their values from the quantum efficiency of the system.

In this case, we determine the quantum efficiency η of the part of system between the qubit-cavity and room-temperature electronics by performing weak measurements on the qubit with coherent light. It is related to η_a by

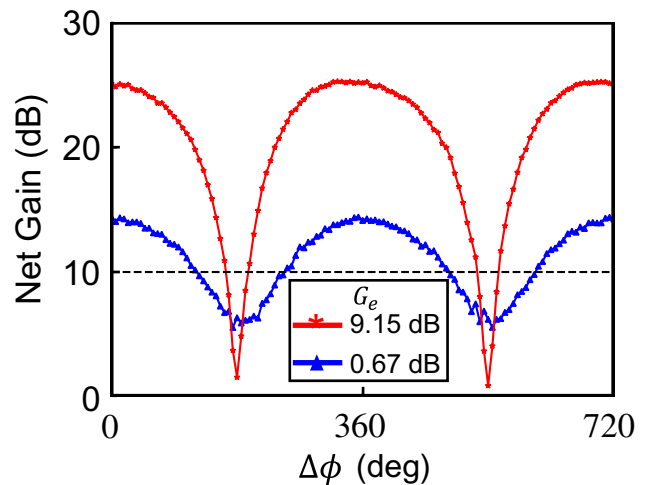$$\eta = \eta_a \eta_{\text{out}}, \qquad \text{(A25)}$$

FIG. 10. Transmission measurement of the S parameter S_{aa} of the TMS interferometer as a function of the relative pump phase. The gain of the analyzer JPC, G_A, is fixed to be 10 dB during the measurement (to avoid gain saturation for large entangler gain settings), as shown by the black dashed line. The blue triangle and red star traces correspond to the different gains of the entangler JPC.

where η_{out} is the quantum efficiency of the output line, which is dominated by the quantum efficiency of HEMT. From the weak measurement (next section), we find that $\eta = 0.52$ (0.46 without correction of the qubit T_2 effect).

The quantum efficiency of the output line is directly related to the added noise photon number of the output line N_{out} by

$$\eta_{\text{out}} = \frac{\sigma^2}{\sigma^2 + N_{\text{out}}}, \tag{A26}$$

where σ^2 is the output noise photon number of the analyzer. The added noise photon number of the output line is determined from the noise visibility ratio (NVR) of the system, which is defined as

$$\text{NVR} = \frac{\sigma^2 + N_{\text{out}}}{1/2 + N_{\text{out}}}, \tag{A27}$$

the ratio between the output noise power with the analyzer on and that with the analyzer off while only vacuum noise is present at its input.

In our experiment, the NVR is measured to be 7 dB when the analyzer gain is 20 dB. Under the assumption that the analyzer is quantum limited, we get $N_{\text{out}} = 24.8$, which corresponds to a noise temperature of 8.9 K at 7.5 GHz that is typical for such a system. From Eq. (A26), we then get $\eta_{\text{out}} = 0.8$. Combining these results with Eq. (A25), we get $\eta_a = 0.65$. From $\eta_a^2/\eta_b = 0.8$, we get $\eta_b = 0.53$.

With all these parameters determined, we can now directly calculate the normalized output noise and qubit readout SNR and compare them with experimental data. However, as mentioned earlier that analyzer gain varies slightly with the relative pump phase due to entangler pump leakage, we instead use Eqs. (A22) and (A24) to fit the normalized output noise and qubit readout SNR with the analyzer gain as the only fitting parameter, respectively. The fitting curves are shown in Figs. 2(a) and 4(a) with colors corresponding to their respective data sets. Optimal noise suppression and the SNR extracted from the data (color dots) and calculated from Eqs. (A22) and (A24) are shown in Figs. 2(b) and 4(b), respectively. Analyzer gain obtained from these fittings is compared to that obtained from the pump leakage fitting in Fig. 11. Except at $G_E = 4.5$ dB, analyzer gain values from the noise fitting and SNR fitting agrees reasonably well with each other, and are both within the range of gain variation caused by entangler pump leakage. Both fittings give average analyzer gains over the full range of relative pump phases that are expected to be different from the gain with the entangler off (black dots). In addition, analyzer gain obtained from fitting the SNR data is an average of the values for qubits in $|g\rangle$ and $|e\rangle$ that are slight different from each other. Therefore, analyzer gain from noise fitting shows better overall agreement with the experiment value than that from SNR fitting.
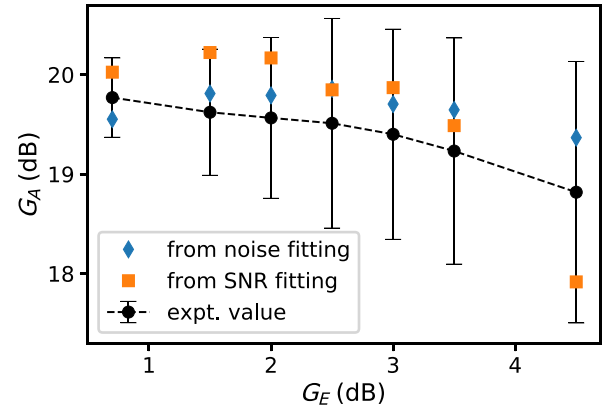

FIG. 11. Fitting value of the analyzer gain (G_A). Analyzer gains (G_A) obtained from fitting the TMS noise data [Fig. 2(a)] and the SNR data [Fig. 4(a)] are shown with blue diamonds and orange squares, respectively. Black dots represent the analyzer gain determined from Fig. 8(a). Error bar for each data point is given by ΔG_A in Fig. 8(b).

5. Back action of the weak measurement

In this section we give a brief introduction of the weak measurement protocol that we use to calibrate the quantum efficiency of our measurement. A quantum measurement will perturb the state of the qubit. This perturbation is known as the back action of the measurement. For a measurement performed with ideal quantum hardware, the qubit will still be in pure state after the measurement, as the evolution of the state can be perfectly tracked from the measurement record. In the usual coherent light measurement scheme, in order to measure a qubit in state $|\psi\rangle = c_g |g\rangle + c_e |e\rangle$, we send a coherent light probe signal to the qubit-cavity system. After the probe signal traverses the cavity, the coherent light and the qubit form a new entangled state together: $|\Psi\rangle = c_g |g\rangle |\alpha_g\rangle + c_e |e\rangle |\alpha_e\rangle$. Here $|\alpha_{g,e}\rangle$ is the transmitted coherent state when the qubit is the ground or excited state, respectively. This new entangled state will serve as the pointer state of the system and will be sent through a quantum limited amplifier (e.g., a JPC) so the signal can be received and processed at room temperature.

The effect of the back action of a phase-preserving measurement can be understood as follows: each shot of outcome will contain the measurements of both quadrature of the output mode, which we denote as (I_m, Q_m). This I-Q pair will be used to determine the state of the qubit after the measurement and, as has been pointed out in Refs [42,45], it contains all the information to track the state evolution of the qubit (provided the measurement is lossless). That is, we can reconstruct the Bloch vector for the qubit after the measurement given the measurement result (I_m, Q_m). However, in an actual experiment, there will also be losses. Therefore, we introduce the concept of measurement efficiency $\eta = (\sigma_{\text{Heis}}^2)/(\sigma_{\text{Heis}}^2 + \sigma_{\text{add}}^2)$ as a way to

measure how much quantum information is collected by the observer. Here σ_{Heis} is the fundamental quantum noise from Heisenberg's uncertainty principle and σ_{add} is the noise added by the amplification chain in the measurement setup. As an example, for a qubit that is initially prepared in state $|+y\rangle = (|g\rangle + |e\rangle)/\sqrt{2}$, the final qubit Bloch vector (x_f, y_f, z_f) is a function of measurement outcome (I_m, Q_m) (for simplicity, we neglect the qubit decoherence and the all losses before the quantum limited amplifier). Hatridge *et al.* [42] found that

$$
x_f(I_m, Q_m) = \operatorname{sech}\left(\frac{I_m \bar{I}_m}{\sigma^2}\right) \sin\left[\frac{Q_m \bar{I}_m}{\sigma^2} + \frac{\bar{Q}_m \bar{I}_m}{\sigma^2}\left(\frac{1-\eta}{\eta}\right)\right]
$$
$$
\times \exp\left\{-\frac{\bar{I}_m^2}{\sigma^2}\left(\frac{1-\eta}{\eta}\right)\right\}, \tag{A28}
$$

$$
y_f(I_m, Q_m) = \operatorname{sech}\left(\frac{I_m \bar{I}_m}{\sigma^2}\right) \cos\left[\frac{Q_m \bar{I}_m}{\sigma^2} + \frac{\bar{Q}_m \bar{I}_m}{\sigma^2}\left(\frac{1-\eta}{\eta}\right)\right]
$$
$$
\times \exp\left\{-\frac{\bar{I}_m^2}{\sigma^2}\left(\frac{1-\eta}{\eta}\right)\right\}, \tag{A29}
$$

$$
z_f(I_m, Q_m) = \tanh\left(\frac{I_m \bar{I}_m}{\sigma^2}\right), \tag{A30}
$$

where $\bar{I}_m$, $\bar{Q}_m$ and σ are the center and standard deviation of 2D Gaussian distribution corresponding to the coherent measurement pulse. The above results indicate that by observing the measurement back action we can obtain the measurement efficiency as a parameter to assess the quality of the measurement apparatus.

We use the pulse sequence shown in Fig. 12 to obtain the measurement back action. We first use a strong projective measurement and record the data from which we postselect to pick out the runs with the qubit found in the ground state. Next, we rotate the qubit into the $|+y\rangle$ state with a $\pi/2$ pulse. Then, we deliberately apply a measurement with a strength weaker than the projective measurement, and record the result. Finally, we do full tomography on the qubit state to determine its Bloch components with another projective measurement. To get the back-action result for a certain weak measurement outcome (I_m, Q_m), the Bloch components of the qubit ($\langle x\rangle_c$, $\langle y\rangle_c$, $\langle z\rangle_c$) are calculated from the tomography result conditioned on recording the specific weak measurement result in a finely binned histogram.

A theoretical result is shown in Fig. 13. When the measurement strength is weak, the ground and excited state distributions largely overlap with each other. Their separation increases as the measurement strength (or SNR) increases. For the strong measurement case, by definition, the two distributions are well separated. The conditional tomography data $\langle X\rangle_c$, $\langle Y\rangle_c$, and $\langle Z\rangle_c$ versus measurement outcome $(I_m/\sigma, Q_m/\sigma)$ is also shown in the figure. When
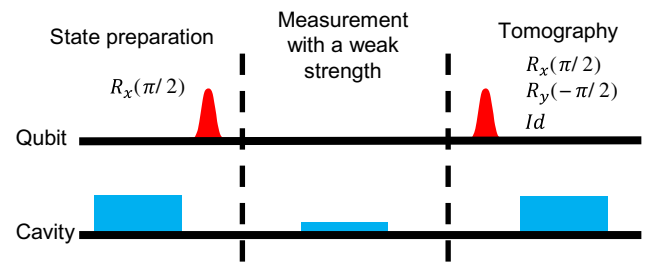

FIG. 12. Pulse sequence for quantifying measurement back action. This pulse sequence comprises three stages of qubit and cavity manipulation. The first stage is state preparation, during which the qubit is first projected to state $|g\rangle$ by a strong measurement (blue box) and postselected, and then rotated to state $(|g\rangle + i|e\rangle)/\sqrt{2}$ by a $R_x(\pi/2)$ pulse (red Gaussian). The second stage is a weak measurement, during which the qubit state is measured by a weak measurement pulse (thin blue box) and an outcome (I_m, Q_m) is recorded. In the third and final stage a qubit state tomography is performed by a combination of qubit rotation pulses (red Gaussian) $R_x(\pi/2)$, $R_y(-\pi/2)$, or Id (no pulse) and a strong measurement (blue box) pulse. Note that a similar pulse sequence is used to record the back action of the noise measurements; see Fig. 3. The only difference in the noise measurement is replacing the middle weak measurement with a record of noise of the system. That is, we apply no cavity drives, but only digitize the output noise of the system.

the measure strength is weak, the qubit state receives minimal perturbation from the measurement, with the outcomes corresponding most probably to Bloch vectors along the $+y$ direction. In practice, any outcome is possible, but outcomes that are very improbable require too many measurements to be practically observed, and so we truncate the theory and set all points to gray, which are more than 2σ away from the centers of the two Gaussian blobs. We can also see the gradients in $\langle X\rangle_c$ along the Q_m axis and $\langle Z\rangle_c$ along the I_m axis, indicating the back action of the measurement. In an actual experiment, after getting these back-action data with this weak measurement protocol, by fitting the x- and y-conditional tomography data for outcomes where the z component is zero (where $I_m = 0$ in the theory plot), we can extract the measurement efficiency as a single fit parameter by comparing the frequency of oscillation (which we can extract from the histogram) to the amplitude of oscillations using the theory expression above.

When the measurement is strong, the qubit is then projected along the $+z$ direction for positive I_m values and $-z$ direction for negative I_m values. The oscillations in $\langle X\rangle_c$ and $\langle Y\rangle_c$ (where the z back action is weak) are still visible very near $I_m = 0$ but are both very improbable (hence nearly being pinched off by our chosen cutoff in the graphs) and very quickly varying, which will be almost impossible to detect in a practical lossy environment with a reasonable
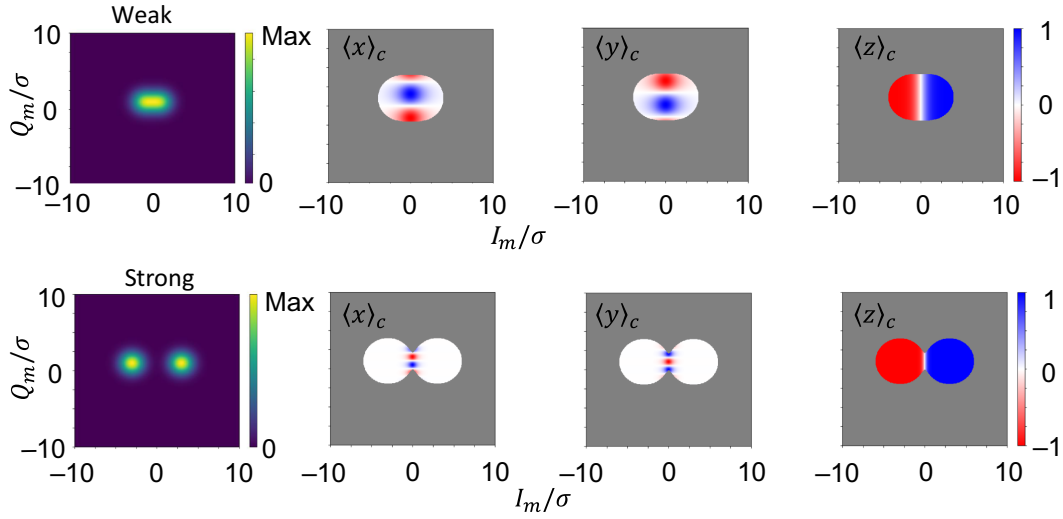
FIG. 13. Theory result for the measurement back action. Theory results for the back action of a "weak" ($\bar{I}_m/\sigma = 1.0$) and "strong" ($\bar{I}_m/\sigma = 3.0$) measurement. The three histograms show $\langle X \rangle_c$, $\langle Y \rangle_c$, and $\langle Z \rangle_c$ versus the associated (I_m/σ, Q_m/σ) bin.

number of repetitions of the protocol. Note that we have set a relatively "weak" projective measurement to make this effect more visible.

Figure 14(a) shows the data of the qubit state tomography for weak measurements with coherent light (top row). This result is similar to what we get from the theoretical model in Fig. 13(b) but with less contrast, which is due to the finite measurement efficiency of the system. Data shown in Fig. 5 are line cuts of the x and y tomography data along $I_m = 0$, where there is no z back action. Oscillation in $\langle x \rangle_c$ and $\langle y \rangle_c$ shows the stochastic phase back action. By fitting the back-action data of a weak measurement to the theory model given in Eqs. (A28), (A29), and (A30), we obtain the overall efficiency for the measurement reported in the paper by comparing the frequency and amplitude of the oscillations.

For TMS light high- and low-matched readout, we can use this protocol to probe the measurement back action. While we lack a full theory for this back action, we are encouraged by the overall outcomes resemblance to "CS + PP with altered noise." Indeed, in Figs. 14(b) and 14(c) we see a close resemblance of the data to CS + PP readout. The strength of the cavity drive is varied such that the separation of the two states in the histograms is the same, so that $\bar{I}_m/\sigma$ match. This should result in a z back action that is indistinguishable for all three case. As shown in Fig. 15 in which we plot a line cut of $\langle z \rangle_c$ through $Q_m = -4$, this is indeed the case. Given that the data do not vary with Q_m, we could also have averaged all data along Q_m to achieve a similar result. However, the x and y back actions, although similar in form, show very different apparent strengths and efficiencies, as discussed in the main text.

6. Noise visibility ratio and quantum efficiency

In this section, we show that the observed large changes in quantum efficiency of the three readout methods *cannot* be explained by changes in the ratio of the output noise of the TMS interferometer and the classical noise from the output chain.

The overall quantum efficiency of the system extracted from the weak measurement protocol can be expressed as

$$\eta = \eta_{\text{Amp}}\, \eta_{\text{out}}, \tag{A31}$$

where η_{Amp} is the efficiency of the system before HEMT (qubit-cavity system and JPC and TMS interferometer) and η_{out} is the efficiency of the output chain after the analyzer JPC that is dominated by the efficiency of the HEMT amplifier. The efficiency of the output chain can be expressed as

$$\eta_{\text{out}} = \frac{N_{\text{Amp}}}{N_{\text{Amp}} + N_{\text{out}}}, \tag{A32}$$

where N_{Amp} is the output noise power of the analyzer JPC and N_{out} is the added noise power of the output chain referred back to the input of the HEMT. An easily measurable quantity in the lab that is closely related to η_{out} is the NVR,

$$\text{NVR} = \frac{N_{\text{Amp}} + N_{\text{out}}}{N_{\text{out}}}. \tag{A33}$$

It is easy to see that

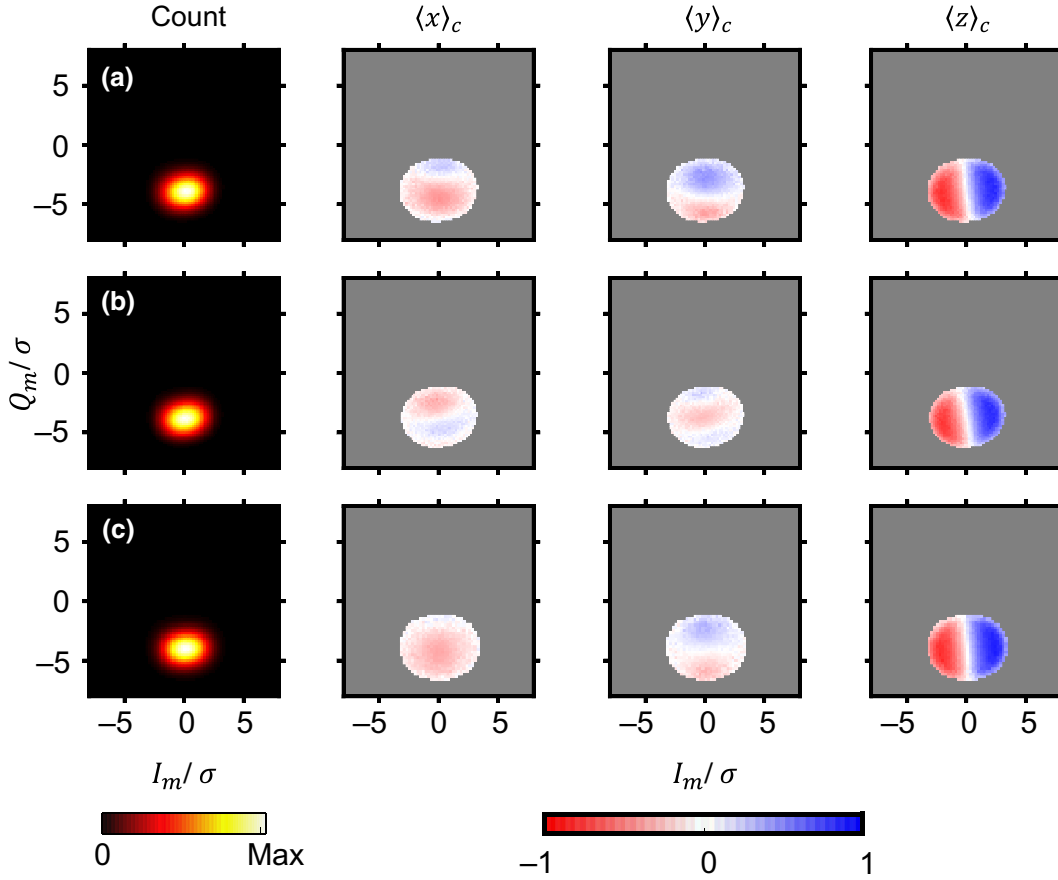$$\eta_{\text{out}} = 1 - \frac{1}{\text{NVR}}. \tag{A34}$$

FIG. 14. Experimental data for back action of the weak measurement. Results are shown for the back action of the weak measurement for coherent light (a) and two-mode squeezed light at high (b) and low (c) noise level match points. In all three cases, the strength of the weak measurement is $\bar{I}_m/\sigma = 0.66$. The leftmost column shows the 2D histograms of scaled measurement outcomes recorded during the weak measurements. The right three columns are the conditional tomography data for the $\langle x \rangle$, $\langle y \rangle$, and $\langle z \rangle$ components versus the associated $(I_m/\sigma, Q_m/\sigma)$ bin. The value in each bin is the average of all tomography data associated with that (I_m, Q_m) value.

In our experiment, the NVR is typically 7 dB when the analyzer JPC is operated at 20-dB gain. Therefore, for coherent light readout, given $\eta = 0.46$ extracted from the weak measurement, we have $\eta_{\text{Amp}} = 0.58$ for our system.

Now consider the case of TMS light. Even though we do not measure the NVR directly, we can calculate it based on the NVR of coherent light and the noise suppression or enhancement shown in Fig. 3. The NVRs for TMS at the high (H) and low (L) match points can be expressed as

$$\text{NVR}_{\text{TMS}}^{H/L} = 1 + \frac{N_{\text{TMS}}^{H/L}}{N_{\text{out}}} = 1 + \frac{N_{\text{CS}}}{N_{\text{out}}} \left(\frac{\sigma_{\text{TMS}}^{H/L}}{\sigma_{\text{CS}}} \right)^2, \quad \text{(A35)}$$

which is larger (smaller) at the high (low) match point than that of coherent light. Consequently, the efficiency of the output chain (η_{out}) will also be larger (smaller) than that of the coherent light readout.

If we assume that the quantum efficiency of the TMS interferometer is the same as that in the coherent light case, namely, $\eta_{\text{Amp}} = 0.58$, and a typical coherent light

NVR, 7 dB, then, given the $(\sigma_{\text{TMSL}}^{H})/\sigma_{\text{CS}} = 1.21$ and $(\sigma_{\text{TMSL}}^{L})/\sigma_{\text{CS}} = 0.86$, we can calculate the overall quantum efficiency of the system at the high and low σ match points.
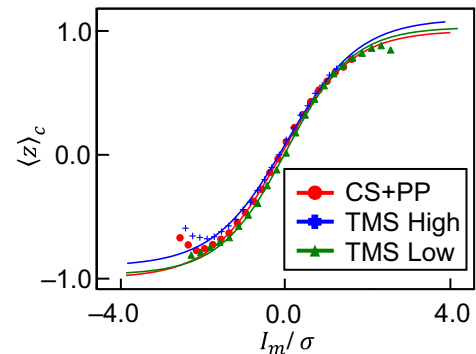

FIG. 15. Experimental data for z-axis back action of the weak measurement. Tomography data for the z component of the qubit Bloch vector along $Q_m = -4$ of the 2D histograms shown in Fig. 14. Different colors indicate the cases CS + PP, "TMS high" match, and "TMS low" match.
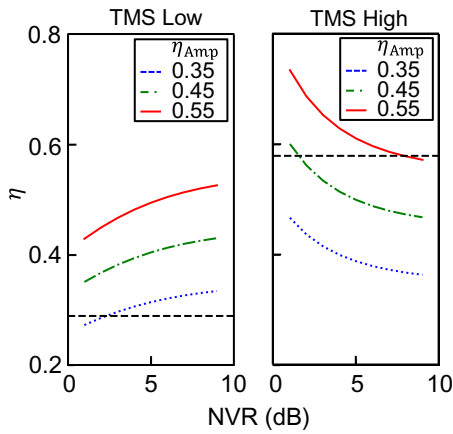
FIG. 16. Calculated overall efficiency of our measurement system for two-mode squeezed light as a function of the NVR for different analyzer JPC/TMS interferometer efficiencies. Overall efficiency of the system versus NVRs at "TMS low" and "TMS high" match points for different amplifier efficiencies $\eta_{\mathrm{Amp}} = 0.35$ (blue dash line), 0.45 (green dotted line), and 0.55 (red line). The black dashed lines show the values of the efficiency obtained from the weak measurement protocol.

We get $\eta^H = 0.48 < \eta^H_{\mathrm{exp}} = 0.58$ and $\eta^L = 0.42 > \eta^L_{\mathrm{exp}} = 0.29$.

More generally, in Fig. 16 we plot the overall efficiency as a function of the NVR for different values of η_{Amp}. It clearly shows that the measured efficiency at "TMS low" and "TML high" match points requires, in addition to changes in the NVR, the analyzer JPC/TMS interferometer to have different quantum efficiencies, which itself requires further study.

[1] Carlton M. Caves, Kip S. Thorne, Ronald W. P. Drever, Vernon D. Sandberg, and Mark Zimmermann, On the measurement of a weak classical force coupled to a quantum-mechanical oscillator. I. Issues of principle, Rev. Mod. Phys. **52**, 341 (1980).

[2] Alexandre Blais, Ren Shou Huang, Andreas Wallraff, S. M. Girvin, and R. J. Schoelkopf, Cavity quantum electrodynamics for superconducting electrical circuits: An architecture for quantum computation, Phys. Rev. A **69**, 1 (2004).

[3] A. A. Clerk, M. H. Devoret, S. M. Girvin, Florian Marquardt, and R. J. Schoelkopf, Introduction to quantum noise, measurement, and amplification, Rev. Mod. Phys. **82**, 1155 (2010).

[4] T. Yamamoto, K. Inomata, M. Watanabe, K. Matsuba, T. Miyazaki, W. D. Oliver, Y. Nakamura, and J. S. Tsai, Flux-driven Josephson parametric amplifier, Appl. Phys. Lett. **93**, 1 (2008).

[5] M. A. Castellanos-Beltran, K. D. Irwin, G. C. Hilton, L. R. Vale, and K. W. Lehnert, Amplification and squeezing of quantum noise with a tunable Josephson metamaterial, Nat. Phys. **4**, 928 (2008).

[6] N. Bergeal, R. Vijay, V. E. Manucharyan, I. Siddiqi, R. J. Schoelkopf, S. M. Girvin, and M. H. Devoret, Analog information processing at the quantum limit with a Josephson ring modulator, Nat. Phys. **6**, 296 (2010).

[7] N. E. Frattini, V. V. Sivak, A. Lingenfelter, S. Shankar, and M. H. Devoret, Optimizing the Nonlinearity and Dissipation of a Snail Parametric Amplifier for Dynamic Range, Phys. Rev. Appl. **10**, 054020 (2018).

[8] Carlton M. Caves, Quantum limits on noise in linear amplifiers, Phys. Rev. D **26**, 1817 (1982).

[9] Google-Quantum-AI, Exponential suppression of bit or phase errors with cyclic error correction, Nature **595**, 383 (2021).

[10] Sebastian Krinner, Nathan Lacroix, Ants Remm, Agustin Di Paolo, Elie Genois, Catherine Leroux, Christoph Hellings, Stefania Lazar, Francois Swiadek, Johannes Herrmann, Graham J. Norris, Christian Kraglund Andersen, Markus Müller, Alexandre Blais, Christopher Eichler, and Andreas Wallraff, Realizing repeated quantum error correction in a distance-three surface code, Nature **605**, 669 (2022).

[11] Nissim Ofek, Andrei Petrenko, Reinier Heeres, Philip Reinhold, Zaki Leghtas, Brian Vlastakis, Yehan Liu, Luigi Frunzio, S. M. Girvin, L. Jiang, Mazyar Mirrahimi, M. H. Devoret, and R. J. Schoelkopf, Extending the lifetime of a quantum bit with error correction in superconducting circuits, Nature **536**, 441 (2016).

[12] V. V. Sivak, A. Eickbusch, B. Royer, S. Singh, I. Tsioutsios, S. Ganjam, A. Miano, B. L. Brock, A. Z. Ding, L. Frunzio, S. M. Girvin, R. J. Schoelkopf, and M. H. Devoret, Real-time quantum error correction beyond break-even, (2022), 10.48550/arXiv.2211.09116.

[13] Alexander P. M. Place *et al.*, New material platform for superconducting transmon qubits with coherence times exceeding 0.3 milliseconds, Nat. Commun. **12**, 1779 (2021).

[14] Chenlu Wang *et al.*, Towards practical quantum computers: Transmon qubit with a lifetime approaching 0.5 milliseconds, Npj Quantum Inf. **8**, 3 (2022).

[15] Aaron Somoroff, Quentin Ficheux, Raymond A. Mencia, Haonan Xiong, Roman V. Kuzmin, and Vladimir E. Manucharyan, Millisecond coherence in a superconducting qubit, (2021), 10.48550/arXiv.2103.08578.

[16] Maxime Boissonneault, J. M. Gambetta, and Alexandre Blais, Dispersive regime of circuit QED: Photon-dependent qubit dephasing and relaxation rates, Phys. Rev. A **79**, 013819 (2009).

[17] U. Vool, I. M. Pop, K. Sliwa, B. Abdo, C. Wang, T. Brecht, Y. Y. Gao, S. Shankar, M. Hatridge, G. Catelani, M. Mirrahimi, L. Frunzio, R. J. Schoelkopf, L. I. Glazman, and M. H. Devoret, Non-Poissonian Quantum Jumps of a Fluxonium Qubit due to Quasiparticle Excitations, Phys. Rev. Lett. **113**, 247001 (2014).

[18] T. Walter, P. Kurpiers, S. Gasparinetti, P. Magnard, A. Potočnik, Y. Salathé, M. Pechal, M. Mondal, M. Oppliger, C. Eichler, and A. Wallraff, Rapid High-Fidelity Single-Shot Dispersive Readout of Superconducting Qubits, Phys. Rev. Appl. **7**, 054020 (2017).

[19] Z. K. Minev, S. O. Mundhada, S. Shankar, P. Reinhold, R. Gutiérrez-Jáuregui, R. J. Schoelkopf, M. Mirrahimi, H. J.

Carmichael, and M. H. Devoret, To catch and reverse a quantum jump mid-flight, Nature **570**, 200 (2019).

[20] Lucas Verney, Raphaël Lescanne, Michel H. Devoret, Zaki Leghtas, and Mazyar Mirrahimi, Structural Instability of Driven Josephson Circuits Prevented by an Inductive Shunt, Phys. Rev. Appl. **11**, 024003 (2019).

[21] Raphaël Lescanne, Lucas Verney, Quentin Ficheux, Michel H. Devoret, Benjamin Huard, Mazyar Mirrahimi, and Zaki Leghtas, Escape of a Driven Quantum Josephson Circuit into Unconfined States, Phys. Rev. Appl. **11**, 014030 (2019).

[22] Alexandru Petrescu, Moein Malekakhlagh, and Hakan E. Türeci, Lifetime renormalization of driven weakly anharmonic superconducting qubits. II. The readout problem, Phys. Rev. B **101**, 134510 (2020).

[23] Moein Malekakhlagh, Alexandru Petrescu, and Hakan E. Türeci, Lifetime renormalization of weakly anharmonic superconducting qubits. I. Role of number nonconserving terms, Phys. Rev. B **101**, 134509 (2020).

[24] Ryo Hanai, Alexander McDonald, and Aashish Clerk, Intrinsic mechanisms for drive-dependent Purcell decay in superconducting quantum circuits, Phys. Rev. Res. **3**, 043228 (2021).

[25] Ross Shillito, Alexandru Petrescu, Joachim Cohen, Jackson Beall, Markus Hauru, Martin Ganahl, Adam G. M. Lewis, Guifre Vidal, and Alexandre Blais, Dynamics of Transmon Ionization, Phys. Rev. Appl. **18**, 034031 (2022).

[26] Jayameenakshi Venkatraman, Xu Xiao, Rodrigo G. Cortiñas, Alec Eickbusch, and Michel H. Devoret, Static Effective Hamiltonian of a Rapidly Driven Nonlinear System, Phys. Rev. Lett. **129**, 100601 (2022).

[27] Michiel Burgelman, Pierre Rouchon, Alain Sarlette, and Mazyar Mirrahimi, Structurally stable subharmonic regime of a driven quantum Josephson circuit, (2022), arXiv:2206.14631 [quant-ph].

[28] Carlton M. Caves, Quantum-mechanical noise in an interferometer, Phys. Rev. D **23**, 1693 (1981).

[29] V Giovannetti, S Lloyd, and L Maccone, Quantum-enhanced measurements: Beating the standard quantum limit, Science **306**, 1330 (2004).

[30] K Goda, O Miyakawa, E. E. Mikhailov, S Saraf, R Adhikari, K McKenzie, R Ward, S Vass, A. J. Weinstein, and N Mavalvala, A quantum-enhanced prototype gravitational-wave detector, Nat. Phys. **4**, 472 (2008).

[31] The-LIGO-Scientific-Collaboration, A gravitational wave observatory operating beyond the quantum shot-noise limit, Nat. Phys. **7**, 962 (2011).

[32] The-LIGO-Scientific-Collaboration, Enhanced sensitivity of the LIGO gravitational wave detector by using squeezed states of light, Nat. Photon. **7**, 613 (2013).

[33] Sh. Barzanjeh, D. P. DiVincenzo, and B. M. Terhal, Dispersive qubit measurement by interferometry with parametric amplifiers, Phys. Rev. B **90**, 134515 (2014).

[34] Nicolas Didier, Jérôme Bourassa, and Alexandre Blais, Fast Quantum Nondemolition Readout by Parametric Modulation of Longitudinal Qubit-Oscillator Interaction, Phys. Rev. Lett. **115**, 203601 (2015).

[35] A. Eddins, S. Schreppler, D. M. Toyli, L. S. Martin, S. Hacohen-Gourgy, L. C. G. Govia, H. Ribeiro, A. A. Clerk, and I. Siddiqi, Stroboscopic Qubit Measurement

with Squeezed Illumination, Phys. Rev. Lett. **120**, 40505 (2018).

[36] S. Touzard, A. Kou, N. E. Frattini, V. V. Sivak, S. Puri, A. Grimm, L. Frunzio, S. Shankar, and M. H. Devoret, Gated Conditional Displacement Readout of Superconducting Qubits, Phys. Rev. Lett. **122**, 080502 (2019).

[37] R. Dassonneville, T. Ramos, V. Milchakov, L. Planat, É. Dumur, F. Foroughi, J. Puertas, S. Leger, K. Bharadwaj, J. Delaforce, C. Naud, W. Hasch-Guichard, J. J. García-Ripoll, N. Roch, and O. Buisson, Fast High-Fidelity Quantum Nondemolition Qubit Readout via a Nonperturbative Cross-Kerr Coupling, Phys. Rev. X **10**, 011045 (2020).

[38] Bernard Yurke, Samuel L. McCall, and John R. Klauder, SU(2) and SU(1, 1) interferometers, Phys. Rev. A **33**, 4033 (1986).

[39] N. Bergeal, F. Schackert, M. Metcalfe, R. Vijay, V. E. Manucharyan, L. Frunzio, D. E. Prober, R. J. Schoelkopf, S. M. Girvin, and M. H. Devoret, Phase-preserving amplification near the quantum limit with a Josephson ring modulator, Nature **465**, 64 (2010).

[40] E. Flurin, N. Roch, F. Mallet, M. H. Devoret, and B. Huard, Generating Entangled Microwave Radiation over Two Transmission Lines, Phys. Rev. Lett. **109**, 1 (2012).

[41] Carlton M. Caves, Joshua Combes, Zhang Jiang, and Shashank Pandey, Quantum limits on phase-preserving linear amplifiers, Phys. Rev. A **86**, 063802 (2012).

[42] M Hatridge, S. Shankar, M. Mirrahimi, F. Schackert, K. Geerlings, T. Brecht, K. M. Sliwa, B. Abdo, L. Frunzio, S. M. Girvin, R. J. Schoelkopf, and M. H. Devoret, Quantum back-action of an individual variable-strength measurement, Science **339**, 178 (2013).

[43] H. Carmichael, *An Open Systems Approach to Quantum Optics* (Springer-Verlag, Berlin, 1993).

[44] H. M. Wiseman and G. J. Milburn, *Quantum Measurement and Control* (Cambridge University Press, Cambridge, 2009).

[45] Alexander N. Korotkov, Quantum Bayesian approach to circuit QED measurement with moderate bandwidth, Phys. Rev. A **94**, 042326 (2016).

[46] C. C. Bultink, B. Tarasinski, N. Haandbæk, S. Poletto, N. Haider, D. J. Michalak, A. Bruno, and L. DiCarlo, General method for extracting the quantum efficiency of dispersive qubit readout in circuit QED, Appl. Phys. Lett. **112**, 092601 (2018).

[47] Carlton M. Caves and Bonny L. Schumaker, New formalism for two-photon quantum optics. I. Quadrature phases and squeezed states, Phys. Rev. A **31**, 3068 (1985).

[48] Christopher C. Gerry, Two-mode squeezed pair coherent states, J. Mod. Opt. **42**, 585 (1995).

[49] R. Loudon and P. L. Knight, Squeezed light, J. Mod. Opt. **34**, 709 (1987).

[50] N. Bergeal, F. Schackert, L. Frunzio, and M. H. Devoret, Two-Mode Correlation of Microwave Quantum Noise Generated by Parametric Down-Conversion, Phys. Rev. Lett. **108**, 123902 (2012).

[51] N. Roch, M. E. Schwartz, F. Motzoi, C. Macklin, R. Vijay, A. W. Eddins, A. N. Korotkov, K. B. Whaley, M. Sarovar, and I. Siddiqi, Observation of Measurement-Induced Entanglement and Quantum Trajectories of Remote Superconducting Qubits, Phys. Rev. Lett. **112**, 170501 (2014).

[52] K. W. Murch, S. J. Weber, C. Macklin, and I. Siddiqi, Observing single quantum trajectories of a superconducting quantum bit, Nature **502,** 211 (2013).

[53] S. Shankar, M. Hatridge, Z. Leghtas, K. M. Sliwa, A. Narla, U. Vool, S. M. Girvin, L. Frunzio, M. Mirrahimi, and M. H. Devoret, Autonomously stabilized entanglement between two superconducting quantum bits, Nature **504,** 419 (2013).

[54] Katrina Sliwa, *Improving the quality of Heisenberg back-action of qubit measurements made with parametric amplifiers* (Yale University, New Haven, CT, 2016).

[55] Martina Esposito, Arpit Ranadive, Luca Planat, Sébastien Leger, Dorian Fraudet, Vincent Jouanny, Olivier Buisson, Wiebke Guichard, Cécile Naud, José Aumentado, Florent Lecocq, and Nicolas Roch, Observation of Two-Mode Squeezing in a Traveling Wave Parametric Amplifier, Phys. Rev. Lett. **128,** 153603 (2022).

[56] Jack Y. Qiu, Arne Grimsmo, Kaidong Peng, Bharath Kannan, Benjamin Lienhard, Youngkyu Sung, Philip Krantz, Vladimir Bolkhovsky, Greg Calusine, David Kim, Alex Melville, Bethany M. Niedzielski, Jonilyn Yoder, Mollie E. Schwartz, Terry P. Orlando, Irfan Siddiqi, Simon Gustavsson, Kevin P. O'Brien, and William D. Oliver, Broadband squeezed microwaves and amplification with a Josephson traveling-wave parametric amplifier, (2022), 10.48550/arXiv.2201.11261.

[57] Tanay Roy, Suman Kundu, Madhavi Chand, A. M. Vadiraj, A. Ranadive, N. Nehra, Meghan P. Patankar, J. Aumentado, A. A. Clerk, and R. Vijay, Broadband parametric amplification with impedance engineering: Beyond the gain-bandwidth product, Appl. Phys. Lett. **107,** 262601 (2015).

[58] Yoshiro Urade, Kun Zuo, Syotaro Baba, C. W. Sandbo Change, Kohichi Nittoh, Kunihiro. Inomata, Zhirong. Lin, Tsuyoshi Yamamoto, and Nakamura Yasunobu, Flux-driven impedance-matched Josephson parametric amplifier with improved pump efficiency, American Physical Society March Meeting, A28.00010 (2021).

[59] Matti Silveri, Evan Zalys-Geller, Michael Hatridge, Zaki Leghtas, Michel H. Devoret, and S. M. Girvin, Theory of remote entanglement via quantum-limited phase-preserving amplification, Phys. Rev. A **93,** 1 (2016).

[60] C. Dickel, J. J. Wesdorp, N. K. Langford, S. Peiter, R. Sagastizabal, A. Bruno, B. Criger, F. Motzoi, and L. DiCarlo, Chip-to-chip entanglement of transmon qubits using engineered measurement fields, Phys. Rev. B **97,** 1 (2018).